SIAM J. SCI. COMPUT.
Vol. 26, No. 3, pp. 1057–1088

EFFICIENT AND STABLE NUMERICAL METHODS FOR THE GENERALIZED AND VECTOR ZAKHAROV SYSTEM*

WEIZHU BAO† AND FANGFANG SUN†

Abstract. We present efficient and stable numerical methods for approximations of the generalized Zakharov system (GZS) and vector Zakharov system for multicomponent plasma (VZSM) with/without a linear damping term. The key points in the methods are based on (i) a time-splitting discretization of a Schrödinger-type equation in GZS or VZSM, (ii) discretizing a nonlinear wave-type equation by a pseudospectral method for spatial derivatives, and (iii) solving the ordinary differential equations (ODEs) in phase space analytically under appropriate chosen transmission conditions between different time intervals or applying Crank–Nicolson/leap-frog for linear/nonlinear terms for time derivatives. The methods are explicit, unconditionally stable, and of spectral-order accuracy in space and second-order accuracy in time. Moreover, they are time reversible and time transverse invariant when there is no damping term in GZS or VZSM, conserve (or keep the same decay rate of) the wave energy as that in GZS or VZSM without a (or with a linear) damping term, and give exact results for the plane-wave solution. Extensive numerical tests are presented for plane waves and solitary-wave collisions in one-dimensional GZS, and we also give the dynamics of three-dimensional VZSM to demonstrate our new efficient and accurate numerical methods. Furthermore, the methods are applied to study the convergence and quadratic convergence rates of VZSM to GZS and of GZS to the nonlinear Schrödinger (NLS) equation in the "subsonic limit" regime ($0 < \varepsilon \ll 1$), where the parameter ε is inversely proportional to the acoustic speed. Our tests also suggest that the following meshing strategy (or ε-resolution) is admissible in this regime: spatial mesh size $h = O(\varepsilon)$ and time step $k = O(\varepsilon)$.

Key words. generalized Zakharov system, subsonic limit, meshing strategy, time reversible, time transverse invariant, unconditionally stable, nonlinear Schrödinger equation

AMS subject classifications. 35Q55, 65T40, 65N12, 65N35, 81-08

DOI. 10.1137/030600941

1. Introduction. In this paper, we present new numerical methods for the generalized Zakharov system (GZS) describing the propagation of Langmuir waves in plasma:

$$i\,\partial_t E + \Delta\, E - \alpha N\, E + \lambda |E|^2\, E + i\gamma\, E = 0, \qquad \mathbf{x} \in \mathbb{R}^d, \quad t > 0, \tag{1.1}$$

$$\varepsilon^2 \partial_{tt} N - \Delta(N - \nu |E|^2) = 0, \qquad \mathbf{x} \in \mathbb{R}^d, \quad t > 0, \tag{1.2}$$

$$E(\mathbf{x}, 0) = E^{(0)}(\mathbf{x}), \quad N(\mathbf{x}, 0) = N^{(0)}(\mathbf{x}), \quad \partial_t N(\mathbf{x}, 0) = N^{(1)}(\mathbf{x}), \quad \mathbf{x} \in \mathbb{R}^d, \tag{1.3}$$

where the complex unknown function $E(\mathbf{x}, t)$ is the slowly varying envelope of the highly oscillatory electric field, the real unknown function $N(\mathbf{x}, t)$ is the deviation of the ion density from its equilibrium value, ε is a parameter inversely proportional to the acoustic speed, $\gamma \geq 0$ is a damping parameter, and α, λ, ν are all real parameters. The GZS is time reversible and time transverse invariant if $\gamma = 0$ in (1.1). In fact, the standard Zakharov system (ZS), i.e., $\varepsilon = 1$, $\nu = -1$, $\lambda = 0$, $\gamma = 0$ in (1.1) and (1.2), was derived by Zakharov [30] for governing the coupled dynamics of the electric-field amplitude and the low-frequency density fluctuations of ions. It has subsequently

*Received by the editors February 10, 2004; accepted for publication (in revised form) April 1, 2004; published electronically February 3, 2005.
http://www.siam.org/journals/sisc/26-3/60094.html

†Department of Computational Science, National University of Singapore, Singapore 117543 (bao@cz3.nus.edu.sg, http://www.cz3.nus.edu.sg/~bao/; sunff@cz3.nus.edu.sg). The research of the first author was supported by National University of Singapore grant R-151-000-027-112.

become commonly accepted that ZS is a general model for governing interaction of a dispersive wave and a nondispersive (acoustic) wave. It has important applications in plasma physics (interactions between Langmuir and ion acoustic waves [30, 25]), in the theory of molecular chains (the interaction of the intramolecular vibrations forming Davydov solitons with the acoustic disturbances in the chain [12]), in hydrodynamics (interactions between short-wave and long-wave gravitational disturbances in the atmosphere [26, 13]), and so on. In three spatial dimensions, ZS was also derived to model the collapse of caverns [30]. Later, the standard ZS was extended to GZS [18, 19], the vector Zakharov system (VZS) [28], and the vector Zakharov system for multicomponents (VZSM) [18, 19].

The global existence of weak solutions of ZS in one dimension is proven in [27, 7, 28], and the existence and uniqueness of smooth solutions for the equations are obtained on the grounds that smooth initial data are prescribed. The well-posedness of ZS was recently improved in [7, 8] for one, two, and three dimensions, and extended for the case with generalized nonlinearity in [11, 14].

Numerical methods for the standard ZS have been studied in the last two decades. Payne, Nicholson, and Downie [24] proposed a Fourier spectral method, in which only two-thirds of the Fourier components were used on a particular mesh in the fast Fourier transform (in fact, this is equivalent to using a numerical filter) in order to suppress the aliasing errors in their algorithm [24]. Of course, this is not an "optimal" way to use the spectral method. In [15, 16], Glassey presented an energy-preserving implicit finite difference scheme for the system and proved its convergence. Later, Chang and Jiang [9] considered an implicit or semiexplicit conservative finite difference scheme for the ZS and proved its convergence; Chang, Guo, and Jiang extended their method for GZS [10]. One can find more numerical study of soliton-soliton collisions using GZS in [22, 18, 19]. For the finite difference methods of ZS with the best combination of time and space discretizations, one needs the following constraints in order to guarantee good numerical approximations in the "subsonic limit" regime, i.e., $0 < \varepsilon \ll 1$:

$$\text{mesh size } h = o(\varepsilon), \qquad \text{time step } k = o(h\varepsilon).$$

Failure to satisfy these conditions leads to wrong numerical solutions [6]. Recently, Bao, Sun, and Wei [6] and Sun [29] presented an explicit numerical method for GZS [6] and VZSM [29]. Their method is time reversible and time transverse invariant when there is no damping term in GZS, keeps the same decay rate of the wave energy as that in the GZS, and gives exact results for the plane-wave solution [6, 29]. They showed the following meshing strategy, which guarantees good numerical approximations for ε small [6] because the method is of spectral-order accuracy in space and its stability constraint:

$$h = O(\varepsilon), \qquad k = O(h\varepsilon) = O(\varepsilon^2).$$

The aim of this paper is to present new numerical methods for GZS and VZSM, which are explicit, unconditionally stable, and of spectral-order accuracy in space and second-order accuracy in time. Moreover, they are time reversible and time transverse invariant when there is no damping term in GZS or VZSM, conserve (or keep the same decay rate of) the wave energy as that in GZS or VZSM without (or with) a linear damping term, and give exact results for the plane-wave solution. More importantly, compared to that of the method in [6, 29] when ε is small, the new methods have an improved meshing strategy for initial data with $O(\varepsilon)$ wavelength:

$$h = O(\varepsilon), \qquad k = O(\varepsilon).$$

In fact, the key points in designing the new numerical methods are based on (i) solving a nonlinear wave-type equation in GZS or VZSM in phase space analytically under appropriate chosen transmission conditions between different time intervals, where this kind of discretization for time derivatives is different from the method for GZS used in [6], and (ii) a time-splitting discretization of a Schrödinger-type equation [1, 2, 3, 4] in GZS or VZSM.

The paper is organized as follows. In section 2 we present the VZSM; simplify it to get the generalized vector Zakharov system (GVZS), standard VZS, GZS, and standard ZS; reduce it to the vector nonlinear Schrödinger (VNLS) equation and NLS equation; and generalize it with a linear damping term to arrest blowup. In section 3 we present new numerical methods for GZS. In section 4 we extend these methods to VZSM. In section 5 numerical tests are reported for GZS and VZSM. In section 6 some conclusions are drawn.

2. The vector Zakharov system (VZS). In this section, we present VZSM, reduction from VZSM to GVZS, from GVZS to GZS, from GVZS to the VNLS equation, from GZS to the NLS equation, and generalization of GZS or GVZS with a linear damping term to arrest blowup.

2.1. The VZS for multicomponent plasma (VZSM). The standard VZS can be derived [28] from the two-fluid model governing a plasma as two interpenetrating fluids combining an electron fluid and an ion fluid by multiple-scale modulation analysis:

$$i\, \partial_t \mathbf{E} + a\, \Delta \mathbf{E} + (1-a)\, \nabla(\nabla \cdot \mathbf{E}) - N\, \mathbf{E} = 0, \tag{2.1}$$

$$\varepsilon^2\, \partial_{tt} N - \Delta N = \Delta |\mathbf{E}|^2, \qquad \mathbf{x} \in \mathbb{R}^d, \quad t > 0, \tag{2.2}$$

where $d = 1, 2$, or 3; $\mathbf{x} = (x_1, \ldots, x_d)^T$ is the Cartesian coordinate; the complex unknown vector function $\mathbf{E}(\mathbf{x}, t) = (E_1(\mathbf{x}, t), \ldots, E_d(\mathbf{x}, t))^T$ is the slowly varying envelope of the highly oscillatory electric field; $N = N(\mathbf{x}, t)$ is the deviation of the ion density from its equilibrium value; and $a > 0$ is a positive constant. The VZS (2.1), (2.2) is commonly used to govern the coupled dynamics of the complex envelope of the electric field oscillations near the electron plasma frequency and the low-frequency density fluctuations of the ions. When $d = 3$, (2.1) is also written as (see [28])

$$i\, \partial_t \mathbf{E} - a \nabla \times (\nabla \times \mathbf{E}) + \nabla(\nabla \cdot \mathbf{E}) - N\, \mathbf{E} = 0. \tag{2.3}$$

The VZS (2.1), (2.2) can be easily generalized to a physical situation when the dispersive waves interact with $\mathcal{M}$ different acoustic modes, e.g., in a multicomponent plasma, which may be described by the following VZSM [28, 18, 19]:

$$i\, \partial_t \mathbf{E} + a\, \Delta \mathbf{E} + (1-a)\, \nabla(\nabla \cdot \mathbf{E}) - \mathbf{E} \sum_{J=1}^{\mathcal{M}} N_J = 0, \quad \mathbf{x} \in \mathbb{R}^d, \quad t > 0, \tag{2.4}$$

$$\varepsilon_J^2\, \partial_{tt} N_J - \Delta N_J + \nu_J\, \Delta |\mathbf{E}|^2 = 0, \quad J = 1, \ldots, \mathcal{M}, \tag{2.5}$$

where the real unknown function N_J is the Jth-component deviation of the ion density from its equilibrium value, $\varepsilon_J > 0$ is a parameter inversely proportional to the acoustic speed of the Jth-component, and ν_J are real constants.

The VZSM (2.4), (2.5) is time reversible and time transverse invariant, and preserves the following three conserved quantities. They are the wave energy

$$D^{VZSM} = \int_{\mathbb{R}^d} |\mathbf{E}(\mathbf{x}, t)|^2\, d\mathbf{x}, \tag{2.6}$$

the momentum

$$\mathbf{P}^{VZSM} = \int_{\mathbb{R}^d} \left[\frac{i}{2} \sum_{j=1}^{d} \left(E_j\, \nabla \overline{E_j} - \overline{E_j}\, \nabla E_j \right) - \sum_{J=1}^{\mathcal{M}} \frac{\varepsilon_J^2}{\nu_J} N_J \mathbf{V_J} \right] d\mathbf{x}, \tag{2.7}$$

and the Hamiltonian

$$\begin{aligned} H^{VZSM} = \int_{\mathbb{R}^d} \Bigg[& a\, \|\nabla \mathbf{E}\|_{l^2}^2 + (1-a)|\nabla \cdot \mathbf{E}|^2 + \sum_{J=1}^{\mathcal{M}} N_J |\mathbf{E}|^2 \\ & - \frac{1}{2} \sum_{J=1}^{\mathcal{M}} \left(\frac{\varepsilon_J^2}{\nu_J} |\mathbf{V}_J|^2 + \frac{1}{\nu_J} N_J^2 \right) \Bigg] d\mathbf{x}, \end{aligned} \tag{2.8}$$

where here and in the following $\bar{f}$ denotes the conjugate of any function f, and the flux vector $\mathbf{V_J} = ((v_J)_1, \ldots, (v_J)_d)^T$ for the Jth component is introduced through the equations

$$\partial_t N_J = -\nabla \cdot \mathbf{V}_J, \quad \partial_t \mathbf{V}_J = -\frac{1}{\varepsilon_J^2} \nabla (N_J - \nu_J |\mathbf{E}|^2), \qquad J = 1, \ldots, \mathcal{M}. \tag{2.9}$$

2.2. Reduction from VZSM to GVZS. In the VZSM (2.4)–(2.5), if we choose $\mathcal{M} = 2$ and assume that $1/\varepsilon_2^2 \gg 1/\varepsilon_1^2$, i.e., that the acoustic speed of the second component is much faster than that of the first component, then formally the fast nondispersive component N_2 can be excluded by means of the relation

$$N_2 = \nu_2\, |\mathbf{E}|^2 + \varepsilon_2^2\, \Delta^{-1} \partial_{tt} N_2 \approx \nu_2\, |\mathbf{E}|^2 + O(\varepsilon_2^2) \qquad \text{when } \varepsilon_2 \to 0. \tag{2.10}$$

Plugging (2.10) into (2.4), the VZSM (2.4), (2.5) is reduced to GVZS with $N = N_1$, $\nu = \nu_1$, $\varepsilon = \varepsilon_1$, $\lambda = -\nu_2$, and $\alpha = 1$:

$$i\, \partial_t \mathbf{E} + a\, \Delta \mathbf{E} + (1-a)\, \nabla(\nabla \cdot \mathbf{E}) - \alpha\, N\, \mathbf{E} + \lambda\, |\mathbf{E}|^2 \mathbf{E} = 0, \tag{2.11}$$

$$\varepsilon^2 \partial_{tt} N - \Delta N + \nu \Delta |\mathbf{E}|^2 = 0, \qquad \mathbf{x} \in \mathbb{R}^d, \quad t > 0. \tag{2.12}$$

The GVZS (2.11), (2.12) is time reversible, time transverse invariant, and preserves the following three conserved quantities, i.e., the wave energy, momentum, and Hamiltonian:

$$D^{GVZS} = \int_{\mathbb{R}^d} |\mathbf{E}(\mathbf{x}, t)|^2\, d\mathbf{x}, \tag{2.13}$$

$$\mathbf{P}^{GVZS} = \int_{\mathbb{R}^d} \left[\frac{i}{2} \sum_{j=1}^{d} \left(E_j\, \nabla \overline{E_j} - \overline{E_j}\, \nabla E_j \right) - \frac{\alpha \varepsilon^2}{\nu} N \mathbf{V} \right] d\mathbf{x}, \tag{2.14}$$

$$\begin{aligned} H^{GVZS} = \int_{\mathbb{R}^d} \Bigg[& a\, \|\nabla \mathbf{E}\|_{l^2}^2 + (1-a)|\nabla \cdot \mathbf{E}|^2 + \alpha N |\mathbf{E}|^2 - \frac{\lambda}{2} |\mathbf{E}|^4 \\ & - \frac{\alpha}{2\nu} N^2 - \frac{\alpha \varepsilon^2}{2\nu} |\mathbf{V}|^2 \Bigg] d\mathbf{x}, \end{aligned} \tag{2.15}$$

where the flux vector $\mathbf{V} = (v_1, \ldots, v_d)^T$ is introduced through the equations

$$\partial_t N = -\nabla \cdot \mathbf{V}, \qquad \partial_t \mathbf{V} = -\frac{1}{\varepsilon^2} \nabla (N - \nu |\mathbf{E}|^2). \tag{2.16}$$

In the case of $\mathcal{M} = 2$, $\nu = \nu_1$; $\varepsilon = \varepsilon_1$, $N = N_1$, and $\mathbf{V} = \mathbf{V}_1$ in (2.7) and (2.8); and $\lambda = -\nu_2$, $\alpha = 1$ in (2.14), (2.15), letting $\varepsilon_2 \to 0$ and noting (2.10), we get a formally quadratic convergence rate of the momentum and Hamiltonian from VZSM to GVZS in the "subsonic limit" regime of the second component, i.e., $0 < \varepsilon_2 \ll 1$:

$$\mathbf{P}^{VZSM} = \int_{\mathbb{R}^d} \left[\frac{i}{2} \sum_{j=1}^{d} \left(E_j \, \nabla \overline{E_j} - \overline{E_j} \, \nabla E_j \right) - \frac{\varepsilon_1^2}{\nu_1} N_1 \mathbf{V} \right] d\mathbf{x} - \frac{\varepsilon_2^2}{\nu_2} \int_{\mathbb{R}^d} N_2 \mathbf{V_2} \, d\mathbf{x}$$

$$\approx \mathbf{P}^{GVZS} + O(\varepsilon_2^2), \tag{2.17}$$

$$H^{VZSM} = \int_{\mathbb{R}^d} \left[a \, \|\nabla \mathbf{E}\|_{l^2}^2 + (1-a)|\nabla \cdot \mathbf{E}|^2 + N_1 |\mathbf{E}|^2 - \frac{1}{2\nu_1} N_1^2 - \frac{\varepsilon_1^2}{2\nu_1} |\mathbf{V_1}|^2 \right] d\mathbf{x}$$
$$+ \int_{\mathbb{R}^d} \left[N_2 |\mathbf{E}|^2 - \frac{1}{2\nu_2} N_2^2 - \frac{\varepsilon_2^2}{2\nu_2} |\mathbf{V_2}|^2 \right] d\mathbf{x}$$

$$\approx H^{GVZS} + O(\varepsilon_2^2). \tag{2.18}$$

Our numerical results in section 5 confirm these results.

Choosing $a = 1$, $\alpha = 1$, $\nu = -1$, and $\lambda = 0$, the GVZS (2.11)–(2.12) collapses to the standard VZS (see [28]):

$$i \, \partial_t \mathbf{E} + \Delta \mathbf{E} - N \mathbf{E} = 0, \qquad \mathbf{x} \in \mathbb{R}^d, \quad t > 0, \tag{2.19}$$

$$\varepsilon^2 \, \partial_{tt} N - \Delta N - \Delta |\mathbf{E}|^2 = 0. \tag{2.20}$$

2.3. Reduction from GVZS to GZS. In the case when $E_2 = \cdots = E_d = 0$ and $a = 1$, the GVZS (2.11)–(2.12) reduces to the scalar GZS [28, 6], i.e., (1.1), (1.2) with $\gamma = 0$:

$$i \, \partial_t E + \Delta E - \alpha \, N \, E + \lambda \, |E|^2 E = 0, \qquad \mathbf{x} \in \mathbb{R}^d, \quad t > 0, \tag{2.21}$$

$$\varepsilon^2 \, \partial_{tt} N - \Delta N + \nu \, \Delta |E|^2 = 0. \tag{2.22}$$

The GZS (2.21), (2.22) is time reversible, time transverse invariant, and conserves the following wave energy, momentum, and Hamiltonian:

$$D^{GZS} = \int_{\mathbb{R}^d} |E(\mathbf{x}, t)|^2 \, d\mathbf{x}, \tag{2.23}$$

$$\mathbf{P}^{GZS} = \int_{\mathbb{R}^d} \left[\frac{i}{2} \left(E \nabla \overline{E} - \overline{E} \nabla E \right) - \frac{\varepsilon^2 \alpha}{\nu} N \mathbf{V} \right] d\mathbf{x}, \tag{2.24}$$

$$H^{GZS} = \int_{\mathbb{R}^d} \left[|\nabla E|^2 + \alpha N |E|^2 - \frac{\lambda}{2} |E|^4 - \frac{\alpha}{2\nu} N^2 - \frac{\alpha \varepsilon^2}{2\nu} |\mathbf{V}|^2 \right] d\mathbf{x}, \tag{2.25}$$

where the flux vector $\mathbf{V} = (v_1, \ldots, v_d)^T$ is introduced through the equations

$$N_t = -\nabla \cdot \mathbf{V}, \qquad \mathbf{V}_t = -\frac{1}{\varepsilon^2} \nabla (N - \nu |E|^2). \tag{2.26}$$

Choosing $\alpha = 1$, $\nu = -1$, $\varepsilon = 1$, and $\lambda = 0$, the GZS (2.21)–(2.22) collapses to the standard ZS [28, 6, 30]. When $\lambda \neq 0$, a cubic nonlinear term is added to the standard ZS.

2.4. Reduction from GVZS to VNLS. In the "subsonic limit," i.e., $\varepsilon \to 0$, which corresponds to the assumption that density fluctuations follow adiabatically the modulation of the Langmuir wave, the GVZS (2.11)–(2.12) collapses to the VNLS equation. In fact, letting $\varepsilon \to 0$ in (2.12), we get formally

$$N = \nu\, |\mathbf{E}|^2 + \varepsilon^2\, \Delta^{-1}\partial_{tt}N = \nu\, |\mathbf{E}|^2 + O(\varepsilon^2) \qquad \text{when } \varepsilon \to 0. \tag{2.27}$$

Plugging (2.27) into (2.11), we obtain formally the VNLS

$$i\, \partial_t \mathbf{E} + a\, \Delta\mathbf{E} + (1-a)\, \nabla(\nabla\cdot\mathbf{E}) + (\lambda - \alpha\nu)|\mathbf{E}|^2\mathbf{E} = 0, \quad \mathbf{x} \in \mathbb{R}^d,\ t > 0. \tag{2.28}$$

The VNLS (2.28) is time reversible, time transverse invariant, and preserves the following wave energy, momentum, and Hamiltonian:

$$D^{VNLS} = \int_{\mathbb{R}^d} |\mathbf{E}(\mathbf{x},t)|^2\, d\mathbf{x}, \tag{2.29}$$

$$\mathbf{P}^{VNLS} = \int_{\mathbb{R}^d} \frac{i}{2}\sum_{j=1}^{d}\left(E_j\, \nabla\overline{E_j} - \overline{E_j}\, \nabla E_j\right)\, d\mathbf{x}, \tag{2.30}$$

$$H^{VNLS} = \int_{\mathbb{R}^d}\left[a\, \|\nabla\mathbf{E}\|_{l^2}^2 + (1-a)|\nabla\cdot\mathbf{E}|^2 + \frac{\alpha\nu-\lambda}{2}|\mathbf{E}|^4\right]\, d\mathbf{x}. \tag{2.31}$$

Letting $\varepsilon \to 0$ in (2.14), (2.15) and noting (2.27), we get formally the quadratic convergence rate of the momentum and Hamiltonian from GVZS to VNLS in the "subsonic limit" regime, i.e., $0 < \varepsilon \ll 1$:

$$\begin{aligned}
\mathbf{P}^{GVZS} &= \int_{\mathbb{R}^d} \frac{i}{2}\sum_{j=1}^{d}\left(E_j\, \nabla\overline{E_j} - \overline{E_j}\, \nabla E_j\right)\, d\mathbf{x} - \frac{\alpha\varepsilon^2}{\nu}\int_{\mathbb{R}^d} N\mathbf{V}\, d\mathbf{x} \\
&\approx \mathbf{P}^{VNLS} + O(\varepsilon^2), \\
H^{GVZS} &= \int_{\mathbb{R}^d}\left[a\, \|\nabla\mathbf{E}\|_{l^2}^2 + (1-a)|\nabla\cdot\mathbf{E}|^2 + \frac{\alpha\nu-\lambda}{2}|\mathbf{E}|^4\right]\, d\mathbf{x} - \frac{\alpha\varepsilon^2}{2\nu}\int_{\mathbb{R}^d} |\mathbf{V}|^2\, d\mathbf{x} \\
&\approx H^{VNLS} + O(\varepsilon^2).
\end{aligned}$$

2.5. Reduction from GZS to NLS. Similarly, in the "subsonic limit," i.e., $\varepsilon \to 0$, the GZS (2.21)–(2.22) collapses to the well-known NLS equation with a cubic nonlinearity. In fact, letting $\varepsilon \to 0$ in (2.22), we get formally

$$N = \nu\, |E|^2 + \varepsilon^2\, \Delta^{-1}\partial_{tt}N = \nu\, |E|^2 + O(\varepsilon^2) \qquad \text{when } \varepsilon \to 0. \tag{2.32}$$

Plugging (2.32) into (2.21), we obtain formally the NLS equation

$$i\, E_t + \Delta\, E + (\lambda - \alpha\nu)|E|^2\, E = 0, \qquad \mathbf{x} \in \mathbb{R}^d, \quad t > 0. \tag{2.33}$$

The NLS equation (2.33) is time reversible, time transverse invariant, and preserves the following wave energy, momentum, and Hamiltonian:

$$D^{NLS} = \int_{\mathbb{R}^d} |E(\mathbf{x},t)|^2\, d\mathbf{x}, \tag{2.34}$$

$$\mathbf{P}^{NLS} = \int_{\mathbb{R}^d}\left[\frac{i}{2}\left(E\nabla\overline{E} - \overline{E}\nabla E\right)\right]\, d\mathbf{x}, \tag{2.35}$$

$$H^{NLS} = \int_{\mathbb{R}^d}\left[|\nabla E|^2 + \frac{\alpha\nu-\lambda}{2}|E|^4\right]\, d\mathbf{x}. \tag{2.36}$$

Similarly, letting $\varepsilon \to 0$ in (2.24), (2.25) and noting (2.32), we get formally the quadratic convergence rate of the momentum and Hamiltonian from GZS to NLS in the "subsonic limit" regime, i.e., $0 < \varepsilon \ll 1$:

$$\begin{aligned} \mathbf{P}^{GZS} &= \int_{\mathbb{R}^d} \frac{i}{2}\left(E\nabla\overline{E} - \overline{E}\nabla E\right)\, d\mathbf{x} - \frac{\varepsilon^2\alpha}{\nu}\int_{\mathbb{R}^d} N\mathbf{V}\, d\mathbf{x} \\ &\approx \mathbf{P}^{NLS} + O(\varepsilon^2), \end{aligned} \tag{2.37}$$

$$\begin{aligned} H^{GZS} &= \int_{\mathbb{R}^d}\left[|\nabla E|^2 + \frac{\alpha\nu-\lambda}{2}|E|^4\right] d\mathbf{x} - \frac{\alpha\varepsilon^2}{2\nu}\int_{\mathbb{R}^d}|\mathbf{V}|^2\, d\mathbf{x} \\ &\approx H^{NLS} + O(\varepsilon^2). \end{aligned} \tag{2.38}$$

Our numerical results in section 5 confirm these results.

2.6. Add a linear damping term to arrest blowup. When $d \geq 2$ and the initial Hamiltonian $H^{GZS} < 0$, mathematically, the GZS (2.21)–(2.22) will blow up in finite time [28, 21]. However, the physical quantities modeled by E and N do not become infinite, which implies that the validity of (2.21), (2.22) breaks down near singularity. Additional physical mechanisms, which were initially small, become important near the singular point and prevent the formation of singularity. In order to arrest blowup, in the physical literature, a small linear damping (absorption) term is introduced into the GZS [17], i.e., (1.1), (1.2):

$$i\,\partial_t E + \Delta E - \alpha\, N\, E + \lambda\, |E|^2 E + i\,\gamma\, E = 0, \tag{2.39}$$

$$\varepsilon^2\, \partial_{tt} N - \Delta N + \nu\, \Delta|E|^2 = 0, \qquad \mathbf{x} \in \mathbb{R}^d, \quad t > 0, \tag{2.40}$$

where $\gamma > 0$ is a damping parameter. The decay rate of the wave energy D^{GZS} of the damped GZS (2.39), (2.40) is

$$\begin{aligned} D^{GZS}(t) &= \int_{\mathbb{R}^d}|E(\mathbf{x},t)|^2\, d\mathbf{x} = e^{-2\gamma t}\int_{\mathbb{R}^d}|E(\mathbf{x},0)|^2\, d\mathbf{x} \\ &= e^{-2\gamma t} D^{GZS}(0), \qquad t \geq 0. \end{aligned} \tag{2.41}$$

Similarly, when $d \geq 2$ and the initial Hamiltonian $H^{GVZS} < 0$ (or $H^{VZSM} < 0$), mathematically, the GVZS (2.11)–(2.12) (or the VZSM (2.4)–(2.5)) will blow up in finite time too. In order to arrest blowup, in the physical literature, a small linear damping (absorption) term is introduced into the GVZS (or VZSM):

$$i\,\partial_t \mathbf{E} + a\,\Delta\mathbf{E} + (1-a)\,\nabla(\nabla\cdot\mathbf{E}) - \alpha\, N\, \mathbf{E} + \lambda\,|\mathbf{E}|^2\mathbf{E} + i\,\gamma\,\mathbf{E} = 0, \tag{2.42}$$

$$\varepsilon^2\partial_{tt} N - \Delta N + \nu\Delta|\mathbf{E}|^2 = 0, \qquad \mathbf{x} \in \mathbb{R}^d, \quad t > 0, \tag{2.43}$$

where $\gamma > 0$ is a damping parameter. The decay rate of the wave energy D^{GVZS} of the damped GVZS (2.42), (2.43) is

$$\begin{aligned} D^{GVZS}(t) &= \int_{\mathbb{R}^d}|\mathbf{E}(\mathbf{x},t)|^2\, d\mathbf{x} = e^{-2\gamma t}\int_{\mathbb{R}^d}|\mathbf{E}(\mathbf{x},0)|^2\, d\mathbf{x} \\ &= e^{-2\gamma t} D^{GVZS}(0), \quad t \geq 0. \end{aligned} \tag{2.44}$$

3. Numerical methods for GZS. In this section we present new numerical methods for the GZS (1.1), (1.2), and (1.3). For simplicity of notation, we shall introduce the method in one space dimension ($d = 1$) of the GZS with periodic boundary conditions. Generalizations to $d > 1$ are straightforward for tensor product grids, and the results remain valid without modifications. For $d = 1$, the problem becomes

$$i\,\partial_t E + \partial_{xx}E - \alpha N\, E + \lambda|E|^2\, E + i\gamma\, E = 0, \quad a < x < b, \quad t > 0, \tag{3.1}$$

$$\varepsilon^2\partial_{tt}N - \partial_{xx}(N - \nu\,|E|^2) = 0, \qquad a < x < b, \quad t > 0, \tag{3.2}$$

$$E(x,0) = E^{(0)}(x), \quad N(x,0) = N^{(0)}(x), \quad \partial_t N(x,0) = N^{(1)}(x), \quad a \le x \le b, \tag{3.3}$$

$$E(a,t) = E(b,t), \qquad \partial_x E(a,t) = \partial_x E(b,t), \qquad t \ge 0, \tag{3.4}$$

$$N(a,t) = N(b,t), \qquad \partial_x N(a,t) = \partial_x N(b,t), \qquad t \ge 0. \tag{3.5}$$

Moreover, we supplement (3.1)–(3.5) by imposing the compatibility condition

$$E^{(0)}(a) = E^{(0)}(b),\ N^{(0)}(a) = N^{(0)}(b),\ N^{(1)}(a) = N^{(1)}(b),\ \int_a^b N^{(1)}(x)\,dx = 0. \tag{3.6}$$

As is well known, the GZS has the following property:

$$\begin{aligned} D^{GZS}(t) &= \int_a^b |E(x,t)|^2\,dx = e^{-2\gamma t}\int_a^b |E^{(0)}(x)|^2\,dx \\ &= e^{-2\gamma t} D^{GZS}(0), \qquad t \ge 0. \end{aligned} \tag{3.7}$$

When $\gamma = 0$, $D^{GZS}(t) \equiv D^{GZS}(0)$, i.e., it is an invariant of the GZS [9]. When $\gamma > 0$, the wave energy $D^{GZS}(t)$ decays to 0 exponentially. Furthermore, the GZS also has the following properties:

$$\int_a^b \partial_t N(x,t)\,dx = 0, \quad \int_a^b N(x,t)\,dx = \int_a^b N^{(0)}(x)\,dx = \text{const.}, \quad t \ge 0. \tag{3.8}$$

In some cases, the boundary conditions (3.4) and (3.5) may be replaced by

$$E(a,t) = E(b,t) = 0, \qquad N(a,t) = N(b,t) = 0, \qquad t \ge 0. \tag{3.9}$$

We choose the spatial mesh size $h = \Delta x > 0$ with $h = (b-a)/M$ for M an even positive integer, the time step $k = \Delta t > 0$, and let the grid points and the time step be

$$x_j := a + j\,h, \qquad j = 0, 1, \ldots, M, \qquad\qquad t_m := m\,k, \qquad m = 0, 1, 2, \ldots.$$

Let E_j^m and N_j^m be the approximations of $E(x_j, t_m)$ and $N(x_j, t_m)$, respectively. Furthermore, let E^m and N^m be the solution vectors at time $t = t_m = mk$ with components E_j^m and N_j^m, respectively.

From time $t = t_m$ to $t = t_{m+1}$, the first NLS-type equation (3.1) is solved in two splitting steps. One solves first

$$i\,\partial_t E + \partial_{xx}E = 0 \tag{3.10}$$

for the time step of length k, followed by solving

$$i\,\partial_t E = \alpha N\,E - \lambda|E|^2\,E - i\gamma\,E \tag{3.11}$$

for the same time step. Equation (3.10) will be discretized in space by the Fourier spectral method and integrated in time *exactly*. For $t \in [t_m, t_{m+1}]$, multiplying (3.11) by $\overline{E}$, we get

$$i\,\partial_t E\,\overline{E} = \alpha N|E|^2 - \lambda|E|^4 - i\gamma|E|^2. \tag{3.12}$$

Then calculating the conjugate of the ODE (3.11) and multiplying it by E, one finds

$$-i\,\partial_t\overline{E}\;E = \alpha N|E|^2 - \lambda|E|^4 + i\gamma|E|^2. \tag{3.13}$$

Subtracting (3.13) from (3.12) and then multiplying both sides by $-i$, one gets

$$\partial_t(|E(x,t)|^2) = \partial_t E(x,t)\overline{E(x,t)} + \partial_t\overline{E(x,t)}E(x,t) = -2\gamma|E(x,t)|^2 \tag{3.14}$$

and therefore

$$|E(x,t)|^2 = e^{-2\gamma(t-t_m)}|E(x,t_m)|^2, \quad t_m \le t \le t_{m+1}. \tag{3.15}$$

Substituting (3.15) into (3.11), we obtain

$$i\partial_t E(x,t) = \alpha N(x,t)E(x,t) - \lambda e^{-2\gamma(t-t_m)}|E(x,t_m)|^2 E(x,t) - i\gamma E(x,t). \tag{3.16}$$

Integrating (3.16) from t_m to t_{m+1}, and then approximating the integral of N on $[t_m, t_{m+1}]$ via the trapezoidal rule, one obtains

$$\begin{aligned} E(x,t_{m+1}) &= e^{-i\int_{t_m}^{t_{m+1}}[\alpha N(x,\tau) - \lambda e^{-2\gamma(\tau-t_m)}|E(x,t_m)|^2 - i\gamma]\,d\tau}\;E(x,t_m) \\ &\approx \begin{cases} e^{-ik[\alpha(N(x,t_m)+N(x,t_{m+1}))/2 - \lambda|E(x,t_m)|^2]}\;E(x,t_m), & \gamma = 0, \\ e^{-\gamma k - i[k\alpha(N(x,t_m)+N(x,t_{m+1}))/2 + \lambda|E(x,t_m)|^2(e^{-2\gamma k}-1)/2\gamma]}\;E(x,t_m), & \gamma \ne 0. \end{cases} \end{aligned}$$

3.1. Crank–Nicolson leap-frog time-splitting spectral discretizations (CN-LF-TSSP). The second wave-type equation (3.2) in the GZS is discretized by a pseudospectral method for spatial derivatives, followed by application of a Crank–Nicolson/leap-frog method for linear/nonlinear terms for time derivatives:

$$\begin{aligned} &\varepsilon^2\frac{N_j^{m+1} - 2N_j^m + N_j^{m-1}}{k^2} - D_{xx}^f\left[\left(\beta N^{m+1} + (1-2\beta)N^m + \beta N^{m-1}\right) - \nu|E^m|^2\right]_{x=x_j} \\ &\qquad = 0, \qquad j = 0,\dots,M, \qquad m = 1,2,\dots, \end{aligned} \tag{3.17}$$

where $0 \le \beta \le 1/2$ is a constant; D_{xx}^f, a spectral differential operator approximation of ∂_{xx}, is defined as

$$D_{xx}^f U\big|_{x=x_j} = -\sum_{l=-M/2}^{M/2-1} \mu_l^2\;\widetilde{U}_l\;e^{i\mu_l(x_j-a)}; \tag{3.18}$$

and $\widetilde{U}_l$, the Fourier coefficients of a vector $U = (U_0, U_1, U_2, \dots, U_M)^T$ with $U_0 = U_M$, are defined as

$$\mu_l = \frac{2\pi l}{b-a}, \quad \widetilde{U}_l = \frac{1}{M}\sum_{j=0}^{M-1} U_j\;e^{-i\mu_l(x_j-a)}, \quad l = -\frac{M}{2},\dots,\frac{M}{2}-1. \tag{3.19}$$

When $\beta = 0$ in (3.17), the discretization (3.17) to the wave-type equation (3.2) is *explicit* and was used in [6, 29]. When $0 < \beta \le 1/2$, the discretization is *implicit*, but can be solved *explicitly*. In fact, suppose

$$N_j^m = \sum_{l=-M/2}^{M/2-1} (\widetilde{N^m})_l\;e^{i\mu_l(x_j-a)}, \qquad j = 0,\dots,M, \quad m = 0,1,\dots. \tag{3.20}$$

Plugging (3.20) into (3.17) and using the orthogonality of the Fourier basis, we obtain

$$\varepsilon^2 \frac{(\widetilde{N^{m+1}})_l - 2(\widetilde{N^m})_l + (\widetilde{N^{m-1}})_l}{k^2}$$
$$+\mu_l^2 \Big[\beta(\widetilde{N^{m+1}})_l + (1-2\beta)(\widetilde{N^m})_l + \beta(\widetilde{N^{m-1}})_l - \nu(\widetilde{|E^m|^2})_l \Big] = 0,$$
$$l = -\frac{M}{2}, \ldots, \frac{M}{2} - 1, \quad m = 1, 2, \ldots. \tag{3.21}$$

Solving the above equation, we get

$$(\widetilde{N^{m+1}})_l = \left(2 - \frac{k^2\mu_l^2}{\varepsilon^2 + \beta k^2 \mu_l^2}\right) (\widetilde{N^m})_l - (\widetilde{N^{m-1}})_l + \frac{\nu k^2 \mu_l^2}{\varepsilon^2 + \beta k^2\mu_l^2} (\widetilde{|E^m|^2})_l,$$
$$l = -\frac{M}{2}, \ldots, \frac{M}{2} - 1, \qquad m = 1, 2, \ldots. \tag{3.22}$$

From time $t = t_m$ to $t = t_{m+1}$, we combine the splitting steps via the standard Strang splitting:

$$N_j^{m+1} = \sum_{l=-M/2}^{M/2-1} (\widetilde{N^{m+1}})_l \; e^{i\mu_l(x_j - a)}, \tag{3.23}$$

$$E_j^* = \sum_{l=-M/2}^{M/2-1} e^{-ik\mu_l^2/2} (\widetilde{E^m})_l \; e^{i\mu_l(x_j-a)},$$

$$E_j^{**} = \begin{cases} e^{-ik[\alpha(N_j^m + N_j^{m+1})/2 - \lambda|E_j^*|^2]} \; E_j^*, & \gamma = 0, \\ e^{-\gamma k - i[k\alpha(N_j^m + N_j^{m+1})/2 + \lambda |E_j^*|^2 (e^{-2\gamma k} - 1)/2\gamma]} \; E_j^*, & \gamma \neq 0, \end{cases}$$

$$E_j^{m+1} = \sum_{l=-M/2}^{M/2-1} e^{-ik\mu_l^2/2} (\widetilde{E^{**}})_l \; e^{i\mu_l(x_j-a)}, \quad 0 \le j \le M-1, \quad m \ge 0, \tag{3.24}$$

where $(\widetilde{N^{m+1}})_l$ is given in (3.22) for $m > 0$ and (3.27) for $m = 0$. The initial conditions (3.3) are discretized as

$$E_j^0 = E^{(0)}(x_j), \quad N_j^0 = N^{(0)}(x_j), \quad \frac{N_j^1 - N_j^{-1}}{2k} = N_j^{(1)}, \quad 0 \le j \le M-1, \tag{3.25}$$

where

$$N_j^{(1)} = \begin{cases} N^{(1)}(x_j), & 0 \le j \le M-2, \\ -\sum_{l=0}^{M-2} N^{(1)}(x_l), & j = M-1. \end{cases} \tag{3.26}$$

This implies that

$$(\widetilde{N^1})_l = \left(1 - \frac{k^2\mu_l^2}{2(\varepsilon^2 + \beta k^2 \mu_l^2)}\right) (\widetilde{N^{(0)}})_l + k\,(\widetilde{N^{(1)}})_l + \frac{\nu k^2\mu_l^2}{2(\varepsilon^2 + \beta k^2 \mu_l^2)} (\widetilde{|E^{(0)}|^2})_l,$$
$$l = -\frac{M}{2}, \ldots, \frac{M}{2} - 1. \tag{3.27}$$

This type of discretization for the initial condition (3.3) is equivalent to using the trapezoidal rule for the periodic function $N^{(1)}$ and is such that the discretized version of (3.8) is satisfied. The discretization error converges to 0 exponentially fast as the mesh size h goes to 0.

Note that the spatial discretization error of the method is of spectral-order accuracy in h and the time discretization error is demonstrated to be second-order accurate in k in section 5 from our numerical results.

3.2. Phase space analytical solver + time-splitting spectral discretizations (PSAS-TSSP). Another way to discretize the second wave-type equation (3.2) in GZS is by using a pseudospectral method for spatial derivatives and then solving the ODEs in phase space analytically under appropriate chosen transmission conditions between different time intervals. From time $t = t_m$ to $t = t_{m+1}$, assume

$$N(x,t) = \sum_{l=-M/2}^{M/2-1} \widetilde{N}_l^m(t)\, e^{i\mu_l(x-a)}, \qquad a \le x \le b, \quad t_m \le t \le t_{m+1}. \tag{3.28}$$

Plugging (3.28) into (3.2) and noticing the orthogonality of the Fourier series, we get the following ODEs:

$$\varepsilon^2 \,\frac{d^2\widetilde{N}_l^m(t)}{d\,t^2} + \mu_l^2 \left[\widetilde{N}_l^m(t) - \nu\,(|\widetilde{E(t_m)}|^2)_l\right] = 0, \qquad t_m \le t \le t_{m+1},\ m \ge 0, \tag{3.29}$$

$$\widetilde{N}_l^m(t_m) = \begin{cases} (\widetilde{N^{(0)}})_l, & m = 0, \\ \widetilde{N}_l^{m-1}(t_m), & m > 0, \end{cases} \qquad l = -\frac{M}{2}, \ldots, \frac{M}{2} - 1. \tag{3.30}$$

For each fixed l $(-M/2 \le l \le M/2 - 1)$, equation (3.29) is a second-order ODE. It needs two initial conditions such that the solution is unique. When $m = 0$ in (3.29), (3.30), we have the initial condition (3.30) and we can pose the other initial condition for (3.29) due to the initial condition (3.3) for the GZS (3.1)–(3.5):

$$\frac{d}{dt}\widetilde{N}_l^0(t_0) = \frac{d}{dt}\widetilde{N}_l^0(0) = (\widetilde{N^{(1)}})_l, \qquad l = -\frac{M}{2}, \ldots, \frac{M}{2} - 1. \tag{3.31}$$

Then the solution of (3.29), (3.30) with $m = 0$ and (3.31) is

$$\widetilde{N}_l^0(t) = \begin{cases} (\widetilde{N^{(0)}})_0 + t\ (\widetilde{N^{(1)}})_0, & l = 0, \\[2ex] \left[(\widetilde{N^{(0)}})_l - \nu(|\widetilde{E^{(0)}}|^2)_l\right] \cos\left(\dfrac{\mu_l\, t}{\varepsilon}\right) + \nu\ (|\widetilde{E^{(0)}}|^2)_l & \\ \quad + \dfrac{\varepsilon}{\mu_l} (\widetilde{N^{(1)}})_l \sin\left(\dfrac{\mu_l\, t}{\varepsilon}\right), & l \ne 0, \end{cases} \tag{3.32}$$

$$0 \le t \le t_1, \quad l = -\frac{M}{2}, \ldots, \frac{M}{2} - 1.$$

But when $m > 0$, we only have one initial condition (3.30). One *can't* simply pose the continuity between $\frac{d}{dt}\widetilde{N}_l^m(t)$ and $\frac{d}{dt}\widetilde{N}_l^{m-1}(t)$ across the time $t = t_m$, because the last term in (3.29) is usually different in two adjacent time intervals $[t_{m-1}, t_m]$ and $[t_m, t_{m+1}]$; i.e., $(|\widetilde{E(t_{m-1})}|^2)_l \ne (|\widetilde{E(t_m)}|^2)_l$. Since our goal is to develop an explicit scheme and we need to linearize the nonlinear term in (3.2) in our discretization (3.29), in general,

$$\frac{d}{dt}\widetilde{N}_l^{m-1}(t_m^-) = \lim_{t\to t_m^-}\frac{d}{dt}\widetilde{N}_l^{m-1}(t) \neq \lim_{t\to t_m^+}\frac{d}{dt}\widetilde{N}_l^{m}(t) = \frac{d}{dt}\widetilde{N}_l^{m}(t_m^+), \quad m\geq 1, \qquad l=-\frac{M}{2},\dots,\frac{M}{2}-1. \tag{3.33}$$

Unfortunately, we don't know the jump $\frac{d}{dt}\widetilde{N}_l^{m}(t_m^+) - \frac{d}{dt}\widetilde{N}_l^{m-1}(t_m^-)$ across the time $t=t_m$. In order to get a unique solution of (3.29), (3.30) for $m>0$, we pose here an additional condition:

$$\widetilde{N}_l^{m}(t_{m-1}) = \widetilde{N}_l^{m-1}(t_{m-1}), \qquad l=-\frac{M}{2},\dots,\frac{M}{2}-1. \tag{3.34}$$

The condition (3.34) is equivalent to posing that the solution $\widetilde{N}_l^m(t)$ on the time interval $[t_m,t_{m+1}]$ of (3.29), (3.30) is also a continuity at the time $t=t_{m-1}$. After a simple computation, we get the solution of (3.29), (3.30) and (3.34) for $m>0$:

$$\widetilde{N}_l^m(t) = \begin{cases} \widetilde{N}_0^{m-1}(t_m) + \dfrac{t-t_m}{k}\left[\widetilde{N}_0^{m-1}(t_m) - \widetilde{N}_0^{m-1}(t_{m-1})\right], & l=0,\\[2ex] \left[\widetilde{N}_l^{m-1}(t_m) - \nu\,(\widetilde{|E^m|^2})_l\right]\cos\left(\dfrac{\mu_l(t-t_m)}{\varepsilon}\right) & \\ +\,\nu\,(\widetilde{|E^m|^2})_l + \dfrac{\sin(\mu_l(t-t_m)/\varepsilon)}{\sin(k\mu_l/\varepsilon)}\left[\widetilde{N}_l^{m-1}(t_m)\cos\left(\dfrac{k\mu_l}{\varepsilon}\right)\right. & \\ \left. -\,\widetilde{N}_l^{m-1}(t_{m-1}) + \nu\left[1-\cos\left(\dfrac{k\mu_l}{\varepsilon}\right)\right](\widetilde{|E^m|^2})_l\right], & l\neq 0, \end{cases}$$
$$t_m\leq t\leq t_{m+1}, \quad l=-\frac{M}{2},\dots,\frac{M}{2}-1. \tag{3.35}$$

From time $t=t_m$ to $t=t_{m+1}$, we combine the splitting steps via the standard Strang splitting:

$$N_j^{m+1} = \sum_{l=-M/2}^{M/2-1}\widetilde{N}_l^m(t_{m+1})\,e^{i\mu_l(x_j-a)}, \tag{3.36}$$
$$E_j^{*} = \sum_{l=-M/2}^{M/2-1} e^{-ik\mu_l^2/2}(\widetilde{E^m})_l\,e^{i\mu_l(x_j-a)},$$
$$E_j^{**} = \begin{cases} e^{-ik[\alpha(N_j^m+N_j^{m+1})/2-\lambda|E_j^*|^2]}\,E_j^*, & \gamma=0,\\ e^{-\gamma k - i[k\alpha(N_j^m+N_j^{m+1})/2+\lambda|E_j^*|^2(e^{-2\gamma k}-1)/2\gamma]}\,E_j^*, & \gamma\neq 0,\end{cases}$$
$$E_j^{m+1} = \sum_{l=-M/2}^{M/2-1} e^{-ik\mu_l^2/2}(\widetilde{E^{**}})_l\,e^{i\mu_l(x_j-a)}, \qquad 0\leq j\leq M-1,\ m\geq 0, \tag{3.37}$$

where

$$
\widetilde{N}_l^m(t_{m+1}) = \begin{cases} \widetilde{(N^{(0)})}_0 + k\, \widetilde{(N^{(1)})}_0, & l=0,\ m=0, \\ \widetilde{(N^{(0)})}_l \cos\left(\frac{k\mu_l}{\varepsilon}\right) + \frac{\varepsilon}{\mu_l}\widetilde{(N^{(1)})}_l \sin\left(\frac{k\mu_l}{\varepsilon}\right) & \\ + \nu\left[1-\cos\left(\frac{k\mu_l}{\varepsilon}\right)\right](\widetilde{|E^{(0)}|^2})_l, & l\neq 0,\ m=0, \\ 2\widetilde{N}_l^{m-1}(t_m)\cos\left(\frac{k\mu_l}{\varepsilon}\right) - \widetilde{N}_l^{m-1}(t_{m-1}) & \\ + 2\nu\left[1-\cos\left(\frac{k\mu_l}{\varepsilon}\right)\right](\widetilde{|E^m|^2})_l, & m\geq 1. \end{cases} \tag{3.38}
$$

The initial conditions (3.3) are discretized as

$$
E_j^0 = E^{(0)}(x_j), \quad N_j^0 = N^{(0)}(x_j), \quad (\partial_t N)_j^0 = N_j^{(1)}, \quad 0\leq j\leq M-1. \tag{3.39}
$$

Note that the spatial discretization error of the above method is again of spectral-order accuracy in h, and the time discretization error is demonstrated to be of second-order accuracy in k in section 5 from our numerical results.

3.3. Properties of the numerical methods.

(i) *Plane wave solution.* If the initial data in (3.3) is chosen as

$$
E^{(0)}(x) = c\, e^{i2\pi l x/(b-a)}, \quad N^{(0)}(x) = d, \quad N^{(1)}(x) = 0, \quad a\leq x\leq b, \tag{3.40}
$$

where l is an integer and c, d are constants, then the GZS (3.1)–(3.5) admits the plane wave solution (see [22])

$$
N(x,t) = d, \qquad a<x<b, \quad t\geq 0, \tag{3.41}
$$

$$
E(x,t) = \begin{cases} c\, e^{i\left(\frac{2\pi l x}{b-a}-\omega t\right)}, \quad \omega = \alpha d + \frac{4\pi^2 l^2}{(b-a)^2} - \lambda c^2, & \gamma = 0, \\ c\, e^{-\gamma t} e^{i\left(\frac{2\pi l x}{b-a}-\omega t - \frac{\lambda c^2}{2\gamma}(e^{-2\gamma t}-1)\right)}, \quad \omega = \alpha d + \frac{4\pi^2 l^2}{(b-a)^2}, & \gamma\neq 0. \end{cases} \tag{3.42}
$$

It is easy to see that in this case our numerical methods CN-LF-TSSP (3.23), (3.24) and PAAS-TSSP (3.36), (3.37) give exact results, provided that $M\geq 2(|l|+1)$.

(ii) *Time transverse invariant.* A main advantage of CN-LF-TSSP and PAAS-TSSP is that if a constant r is added to the initial data $N^0(x)$ in (3.3) when $\gamma=0$ in (3.1), i.e., $N^0(x)\to N^0(x)+r$, then the discrete functions N_j^{m+1} obtained from (3.23) or (3.36) get added by r, i.e., $N_j^{m+1}\to N_j^{m+1}+r$, and E_j^{m+1} obtained from (3.24) or (3.37) get multiplied by the phase factor $e^{-ir(m+1)k}$, which leaves the discrete function $|E_j^{m+1}|^2$ unchanged. This property also holds for the exact solution of GZS but does not hold for the finite difference schemes proposed in [15, 9] and the spectral method proposed in [24].

(iii) *Conservation.* Let $U=(U_0,U_1,\ldots,U_M)^T$ with $U_0=U_M$, $f(x)$ be a periodic function on the interval $[a,b]$, and $\|\cdot\|_{l^2}$ be the usual discrete l^2-norm on the interval (a,b), i.e.,

$$
\|U\|_{l^2} = \sqrt{\frac{b-a}{M}\sum_{j=0}^{M-1}|U_j|^2}, \qquad \|f\|_{l^2} = \sqrt{\frac{b-a}{M}\sum_{j=0}^{M-1}|f(x_j)|^2}. \tag{3.43}
$$

Then we have the following result.

THEOREM 3.1. *The CN-LF-TSSP* (3.23)*,* (3.24) *and PSAS-TSSP* (3.36)*,* (3.37) *for GZS possess the following properties (in fact, they are the discretized version of* (3.7) *and* (3.8)*):*

$$\|E^m\|_{l^2}^2 = e^{-2\gamma t_m}\|E^0\|_{l^2}^2 = e^{-2\gamma t_m}\|E^{(0)}\|_{l^2}^2, \qquad m = 0, 1, 2, \dots, \tag{3.44}$$

$$\frac{b-a}{M}\sum_{j=0}^{M-1}\frac{N_j^{m+1} - N_j^m}{k} = 0, \qquad m = 0, 1, 2, \dots, \tag{3.45}$$

and

$$\frac{b-a}{M}\sum_{j=0}^{M-1} N_j^m = \frac{b-a}{M}\sum_{j=0}^{M-1} N_j^0 = \frac{b-a}{M}\sum_{j=0}^{M-1} N^{(0)}(x_j), \quad m \ge 0. \tag{3.46}$$

Proof. From (3.43), (3.37), and (3.19), using the orthogonality of the discrete Fourier series and noticing the Pasavel equality, we have

$$\begin{aligned}
\frac{M}{b-a}\|E^{m+1}\|_{l^2}^2 &= \sum_{j=0}^{M-1}|E_j^{m+1}|^2 = M\sum_{l=-M/2}^{M/2-1}\left|e^{-ik\mu_l^2/2}(\widetilde{E^{**}})_l\right|^2 \\
&= M\sum_{l=-M/2}^{M/2-1}|(\widetilde{E^{**}})_l|^2 = \sum_{j=0}^{M-1}|E_j^{**}|^2 \\
&= e^{-2\gamma k}\sum_{j=0}^{M-1}|E_j^*|^2 = e^{-2\gamma k}\sum_{j=0}^{M-1}|E_j^m|^2 \\
&= e^{-2\gamma k}\frac{M}{b-a}\|E^m\|_{l^2}^2, \qquad m \ge 0.
\end{aligned} \tag{3.47}$$

Thus (3.44) is obtained from (3.47) by induction. The equalities (3.45) and (3.46) can be obtained in a similar way.

(iv) *Unconditional stability.* By the standard von Neumann analysis for (3.23) and (3.36), noting (3.44), we get that PSAS-TSSP and CN-LF-TSSP with $1/4 \le \beta \le 1/2$ are unconditionally stable, and CN-LF-TSSP with $0 \le \beta < 1/4$ is conditionally stable with stability constraint $k \le \frac{2h\varepsilon}{\pi\sqrt{d(1-4\beta)}}$ in d dimensions ($d = 1, 2, 3$). In fact, for PSAS-TSSP (3.36), (3.37), setting $(\widetilde{|E^m|^2})_l = 0$ and plugging $\widetilde{N}_l^m(t_{m+1}) = \mu\widetilde{N}_l^{m-1}(t_m) = \mu^2\widetilde{N}_l^{m-1}(t_{m-1})$ into (3.38) with $|\mu|$ the amplification factor, we obtain the characteristic equation

$$\mu^2 - 2\cos\left(\frac{k\mu_l}{\varepsilon}\right)\mu + 1 = 0. \tag{3.48}$$

This implies

$$\mu = \cos\left(\frac{k\mu_l}{\varepsilon}\right) \pm i\,\sin\left(\frac{k\mu_l}{\varepsilon}\right). \tag{3.49}$$

Thus the amplification factor

$$G_l = |\mu| = \sqrt{\cos^2\left(\frac{k\mu_l}{\varepsilon}\right) + \sin^2\left(\frac{k\mu_l}{\varepsilon}\right)} = 1, \qquad l = -\frac{M}{2}, \dots, \frac{M}{2} - 1.$$

This, together with (3.44), implies that PSAS-TSSP is unconditionally stable. Similarly for CN-LF-TSSP (3.23), (3.24), noting (3.22), we have the characteristic equation

$$\mu^2 - \left(2 - \frac{k^2\mu_l^2}{\varepsilon^2 + \beta k^2 \mu_l^2}\right)\mu + 1 = 0. \tag{3.50}$$

This implies

$$\mu = 1 - \frac{k^2\mu_l^2}{2(\varepsilon^2 + \beta k^2\mu_l^2)} \pm \sqrt{\left(1 - \frac{k^2\mu_l^2}{2(\varepsilon^2 + \beta k^2\mu_l^2)}\right)^2 - 1}. \tag{3.51}$$

When $1/4 \le \beta \le 1/2$, we have

$$\left|1 - \frac{k^2\mu_l^2}{2(\varepsilon^2 + \beta k^2\mu_l^2)}\right| \le 1, \qquad k > 0, \quad l = -\frac{M}{2}, \dots, \frac{M}{2} - 1.$$

Thus

$$\mu = 1 - \frac{k^2\mu_l^2}{2(\varepsilon^2 + \beta k^2\mu_l^2)} \pm i\sqrt{1 - \left(1 - \frac{k^2\mu_l^2}{2(\varepsilon^2 + \beta k^2\mu_l^2)}\right)^2}. \tag{3.52}$$

This implies the amplification factor

$$\begin{aligned} G_l = |\mu| &= \sqrt{\left(1 - \frac{k^2\mu_l^2}{2(\varepsilon^2 + \beta k^2\mu_l^2)}\right)^2 + 1 - \left(1 - \frac{k^2\mu_l^2}{2(\varepsilon^2 + \beta k^2\mu_l^2)}\right)^2} \\ &= 1, \qquad l = -\frac{M}{2}, \dots, \frac{M}{2} - 1. \end{aligned}$$

This, together with (3.44), implies that CN-LF-TSSP with $1/4 \le \beta \le 1/2$ is unconditionally stable. On the other hand, when $0 \le \beta < 1/4$, we need the stability condition

$$\left|1 - \frac{k^2\mu_l^2}{2(\varepsilon^2 + \beta k^2\mu_l^2)}\right| \le 1 \implies k \le \min_{-M/2 \le l \le M/2-1} \frac{2\varepsilon}{\sqrt{(1-4\beta)\mu_l^2}} = \frac{2h\varepsilon}{\pi\sqrt{1-4\beta}}.$$

This, together with (3.44), implies that CN-LF-TSSP with $0 \le \beta < 1/4$ is conditionally stable in one dimension with stability condition

$$k \le \frac{2h\varepsilon}{\pi\sqrt{1-4\beta}}. \tag{3.53}$$

All above stability results are confirmed by our numerical experiments in section 5.

(v) *ε-resolution in the "subsonic limit" regime* ($0 < \varepsilon \ll 1$). As our numerical results in section 5 suggest, the meshing strategy (or ε-resolution) which guarantees good numerical approximations of our new numerical methods PSAS-TSSP and CN-LF-TSSP with $1/4 \le \beta \le 1/2$ in the "subsonic limit" regime, i.e., $0 < \varepsilon \ll 1$, for initial data in (3.3) with $O(\varepsilon)$ wavelength, is

$$h = O(\varepsilon), \qquad k = O(\varepsilon),$$

where the meshing strategy for CN-LF-TSSP with $0 \le \beta < 1/4$ is

$$h = O(\varepsilon), \qquad k = O(h\varepsilon) = O(\varepsilon^2).$$

Remark 3.1. If the periodic boundary conditions (3.4) and (3.5) are replaced by the homogeneous Dirichlet boundary condition (3.9), then the Fourier basis used in the above algorithm can be replaced by the sine basis [6] or the algorithm in section 4 for VZSM. Similarly, if homogeneous Neumann conditions are used, then a cosine series can be applied in designing the algorithm.

4. Extension to VZS. The idea for constructing the numerical methods CN-LF-TSSP and PSAS-TSSP for GZS (3.1)–(3.5) can be easily extended to the VZSM [29] in three dimensions for $\mathcal{M}$ different acoustic modes in a box $\Omega = [a_1, b_1]\times[a_2, b_2]\times[a_3, b_3]$ with homogeneous Dirichlet boundary conditions:

$$i\partial_t \mathbf{E} + a\,\Delta\mathbf{E} + (1-a)\,\nabla(\nabla\cdot\mathbf{E}) - \alpha\mathbf{E}\sum_{J=1}^{\mathcal{M}} N_J + \lambda|\mathbf{E}|^2\mathbf{E} + i\gamma\mathbf{E} = 0, \tag{4.1}$$

$$\varepsilon_J^2\partial_{tt}N_J - \Delta N_J + \nu_J\Delta|\mathbf{E}|^2 = 0, \quad J=1,\ldots,\mathcal{M}, \qquad \mathbf{x}\in\Omega,\ t>0, \tag{4.2}$$

$$\mathbf{E}(\mathbf{x},0) = \mathbf{E}^{(0)}(\mathbf{x}),\ N_J(\mathbf{x},0) = N_J^{(0)}(\mathbf{x}),\ \partial_t N_J(\mathbf{x},0) = N_J^{(1)}(\mathbf{x}),\ \mathbf{x}\in\Omega, \tag{4.3}$$

$$\mathbf{E}(\mathbf{x},t) = \mathbf{0},\ N_J(\mathbf{x},t) = 0 \qquad (J=1,\ldots,\mathcal{M}), \qquad \mathbf{x}\in\partial\Omega, \tag{4.4}$$

where $\mathbf{x} = (x,y,z)^T$ and $\mathbf{E}(\mathbf{x},t) = (E_1(\mathbf{x},t), E_2(\mathbf{x},t), E_3(\mathbf{x},t))^T$. Moreover, we supplement (4.1)–(4.4) by imposing the compatibility condition

$$\mathbf{E}^{(0)}(\mathbf{x}) = \mathbf{0}, \quad N_J^{(0)}(\mathbf{x}) = N_J^{(1)}(\mathbf{x}) = 0, \quad \mathbf{x}\in\partial\Omega, \quad J=1,\ldots,\mathcal{M}. \tag{4.5}$$

In some cases, the homogeneous Dirichlet boundary condition (4.4) may be replaced by periodic boundary conditions:

$$\text{with periodic boundary conditions for } \mathbf{E}, \quad N_J (J=1,\ldots,\mathcal{M}) \text{ on } \partial\Omega. \tag{4.6}$$

We choose the spatial mesh sizes $h_1 = \frac{b_1-a_1}{M_1}$, $h_2 = \frac{b_2-a_2}{M_2}$, and $h_3 = \frac{b_3-a_3}{M_3}$ in the x-, y-, and z-directions, respectively, with M_1, M_2, and M_3 given positive integers; the time step $k = \Delta t > 0$. Denote grid points and time steps as

$$x_j := a_1 + jh_1,\ j=0,1,\ldots,M_1; \quad y_p := a_2 + ph_2,\ p=0,1,\ldots,M_2;$$
$$z_s := a_3 + sh_3,\ s=0,1,\ldots,M_3; \quad t_m := mk,\ m=0,1,2,\ldots.$$

Let $\mathbf{E}^m_{j,p,s}$ and $(N_J)^m_{j,p,s}$ be the approximations of $\mathbf{E}(x_j, y_p, z_s, t_m)$ and $N_J(x_j, y_p, z_s, t_m)$, respectively.

For simplicity, here we only extend PSAS-TSSP from GZS (3.1)–(3.5) to VZSM (4.1)–(4.4) with homogeneous Dirichlet conditions. For periodic boundary conditions (4.6), extension of CN-LF-TSSP can be done in a similar way. Following the idea of constructing PSAS-TSSP for GZS and the TSSP for VZSM in [29], here we only present the numerical algorithm. From time $t = t_m$ to $t = t_{m+1}$, the PSAS-TSSP method for VZSM (4.1)–(4.4) reads

$$(N_J)^{m+1}_{j,p,s} = \sum_{(l,g,r)\in\mathcal{N}} \widetilde{(N_J)}^m_{l,g,r}(t_{m+1}) \sin\left(\frac{lj\pi}{M_1}\right)\sin\left(\frac{pg\pi}{M_2}\right)\sin\left(\frac{sr\pi}{M_3}\right), \tag{4.7}$$

$$\mathbf{E}^*_{j,p,s} = \sum_{(l,g,r)\in\mathcal{N}} B_{l,g,r}(k/2)\ (\widetilde{\mathbf{E}^m})_{l,g,r} \sin\left(\frac{lj\pi}{M_1}\right)\sin\left(\frac{pg\pi}{M_2}\right)\sin\left(\frac{sr\pi}{M_3}\right),$$

$$\mathbf{E}^{**}_{j,p,s} = \begin{cases} \mathbf{E}^*_{j,p,s}\ \exp\Bigg[ik\lambda|\mathbf{E}^*_{j,p,s}|^2 \\ \qquad\qquad - ik\alpha\displaystyle\sum_{J=1}^{\mathcal{M}} \frac{((N_J)^m_{j,p,s} + (N_J)^{m+1}_{j,p,s})}{2}\Bigg], \quad \gamma = 0, \\ \mathbf{E}^*_{j,p,s}\ \exp\Bigg[-\gamma k - \dfrac{i\lambda|\mathbf{E}^*_{j,p,s}|^2(e^{-2\gamma k}-1)}{2\gamma} \\ \qquad\qquad - ik\alpha\displaystyle\sum_{J=1}^{\mathcal{M}} \frac{((N_J)^m_{j,p,s} + (N_J)^{m+1}_{j,p,s})}{2}\Bigg], \quad \gamma \neq 0, \end{cases}$$

$$\mathbf{E}^{m+1}_{j,p,s} = \sum_{(l,g,r)\in\mathcal{N}} B_{l,g,r}\left(\frac{k}{2}\right) \ (\widetilde{\mathbf{E}^{**}})_{l,g,r} \ \sin\left(\frac{lj\pi}{M_1}\right)\sin\left(\frac{pg\pi}{M_2}\right)\sin\left(\frac{sr\pi}{M_3}\right), \tag{4.8}$$

where

$$\mathcal{N} = \{(l,g,r) \mid 1 \le l \le M_1-1,\ 1 \le g \le M_2-1,\ 1 \le r \le M_3-1\},$$

$$\widetilde{(N_J)}^{m}_{l,g,r}(t_{m+1}) = \begin{cases} \widetilde{(N_J^{(0)})}_{0,0,0} + k\ \widetilde{(N_J^{(1)})}_{0,0,0}, & R_{l,g,r}=0, m=0, \\ \widetilde{(N_J^{(0)})}_{l,g,r}\cos\left(\frac{kR_{l,g,r}}{\varepsilon_J}\right) & \\ \quad + \frac{\varepsilon_J}{R_{l,g,r}}\widetilde{(N_J^{(1)})}_{l,g,r}\sin\left(\frac{kR_{l,g,r}}{\varepsilon_J}\right) & \\ \quad + \nu_J\left[1-\cos\left(\frac{kR_{l,g,r}}{\varepsilon_J}\right)\right](\widetilde{|\mathbf{E}^{(0)}|^2})_{l,g,r}, & R_{l,g,r}\ne 0, m=0, \\ 2\widetilde{(N_J)}^{m-1}_{l,g,r}(t_m)\cos\left(\frac{kR_{l,g,r}}{\varepsilon_J}\right) & \\ \quad + 2\nu_J\left[1-\cos\left(\frac{kR_{l,g,r}}{\varepsilon_J}\right)\right](\widetilde{|\mathbf{E}^{m}|^2})_{l,g,r} & \\ \quad - \widetilde{(N_J)}^{m-1}_{l,g,r}(t_{m-1}), & m \ge 1, \end{cases}$$

and

$$B_{l,g,r}(\tau) = \begin{cases} I_3, & l=g=r=0, \\ e^{-ia\tau R^2_{l,g,r}}\left[I_3 + \frac{e^{-i(1-a)\tau R^2_{l,g,r}}-1}{R^2_{l,g,r}}A_{l,g,r}\right], & \text{otherwise}, \end{cases}$$

with

$$R^2_{l,g,r} = \kappa_l^2+\zeta_g^2+\eta_r^2,\ A_{l,g,r} = \begin{pmatrix} \kappa_l^2 & \kappa_l\zeta_g & \kappa_l\eta_r \\ \kappa_l\zeta_g & \zeta_g^2 & \zeta_g\eta_r \\ \kappa_l\eta_r & \zeta_g\eta_r & \eta_r^2 \end{pmatrix} = \begin{pmatrix} \kappa_l \\ \zeta_g \\ \eta_r \end{pmatrix}\begin{pmatrix} \kappa_l & \zeta_g & \eta_r \end{pmatrix},$$

where I_3 is the 3×3 identity matrix and $\widetilde{\mathbf{U}}_{l,g,r}$, the sine-transform coefficients, are defined as

$$\widetilde{\mathbf{U}}_{l,g,r} = \frac{8}{M_1M_2M_3}\sum_{(l,g,r)\in\mathcal{N}} \mathbf{U}_{j,p,s}\sin\left(\frac{lj\pi}{M_1}\right)\sin\left(\frac{pg\pi}{M_2}\right)\sin\left(\frac{sr\pi}{M_3}\right), \tag{4.9}$$

with

$$\kappa_l = \frac{\pi l}{b_1-a_1},\quad l=1,\dots,M_1-1,\qquad \zeta_g = \frac{\pi g}{b_2-a_2},\quad g=1,\dots,M_2-1,$$
$$\eta_r = \frac{\pi r}{b_3-a_3},\quad r=1,\dots,M_3-1.$$

The initial conditions (4.3) are discretized as

$$\mathbf{E}^0_{j,p,s} = \mathbf{E}^{(0)}(x_j,y_p,z_s),$$
$$(N_J)^0_{j,p,s} = N_J^{(0)}(x_j,y_p,z_s),\quad j=0,\dots,M_1,\ p=0,\dots,M_2,\ s=0,\dots,M_3,$$
$$(\partial_t N_J)^0_{j,p,s} = N_J^{(1)}(x_j,y_p,z_s),\qquad J=1,\dots,\mathcal{M}.$$

The properties of the numerical method for GZS in section 3 are still valid here.

5. Numerical examples. In this section, we present numerical results of GZS with a solitary wave solution in one dimension to compare the accuracy, stability, and ε-resolution of the different methods described in section 3. We also present numerical examples including plane waves and solitary-wave collisions in one-dimensional GZS, as well as the dynamics of three-dimensional VZSM, to demonstrate the efficiency and spectral accuracy of the explicit unconditionally stable numerical method PSAS-TSSP for GZS and VZSM.

In all examples except Example 2, the initial conditions for (1.3) are always chosen such that $|E^0|$, N^0, and $N^{(1)}$ decay to zero sufficiently fast as $|\mathbf{x}| \to \infty$. We always compute on a domain that is large enough that the periodic boundary conditions do not introduce a significant aliasing error relative to the problem in the whole space.

5.1. Comparisons of different methods.

Example 1. The standard ZS with a solitary-wave solution; i.e., we choose $d = 1$, $\alpha = 1$, $\lambda = 0$, $\gamma = 0$, and $\nu = -1$ in (1.1)–(1.3). The well-known solitary-wave solution of the ZS (1.1)–(1.3) in this case is given in [22, 19]:

$$E(x,t) = \sqrt{2B^2(1-\varepsilon^2C^2)}\,\mathrm{sech}(B(x-Ct))\; e^{i[(C/2)x-((C/2)^2-B^2)t]}, \tag{5.1}$$

$$N(x,t) = -2B^2\,\mathrm{sech}^2(B(x-Ct)), \quad -\infty < x < \infty, \quad t \ge 0, \tag{5.2}$$

where B, C are constants. The initial condition is taken as

$$E^{(0)}(x) = E(x,0),\; N^{(0)}(x) = N(x,0),\; N^{(1)}(x,0) = \partial_t N(x,0),\; x \in \mathbb{R}, \tag{5.3}$$

where $E(x,0)$, $N(x,0)$, and $\partial_t N(x,0)$ are obtained from (5.1), (5.2) by setting $t = 0$.

We present computations for two different regimes of the acoustic speed, i.e., $1/\varepsilon$.

Case I. $O(1)$-acoustic speed, i.e., we choose $\varepsilon = 1$, $B = 1$, $C = 0.5$ in (5.1), (5.2). Here we test the spatial and temporal discretization errors, conservation of the conserved quantities as well as the stability constraint of different numerical methods. We solve the problem on the interval $[-32, 32]$; i.e., $a = -32$ and $b = 32$ with periodic boundary conditions. Let $E_{h,k}$ and $N_{h,k}$ be the numerical solution of (1.1), (1.2) in one dimension with the initial condition (5.3) by using a numerical method with mesh size h and time step k. To quantify the numerical methods, we define the error functions as

$$e_1 = \|E(\cdot,t) - E_{h,k}(t)\|_{l^2}, \qquad e_2 = \|N(\cdot,t) - N_{h,k}(t)\|_{l^2},$$

$$e = \frac{\|E(\cdot,t) - E_{h,k}(t)\|_{l^2}}{\|E(\cdot,t)\|_{l^2}} + \frac{\|N(\cdot,t) - N_{h,k}(t)\|_{l^2}}{\|N(\cdot,t)\|_{l^2}} = \frac{e_1}{\|E(\cdot,t)\|_{l^2}} + \frac{e_2}{\|N(\cdot,t)\|_{l^2}}$$

and evaluate the conserved quantities D^{GZS}, P^{GZS}, and H^{GZS} by using the numerical solution, i.e., replacing E and N by their numerical counterparts $E_{h,k}$ and $N_{h,k}$, respectively, in (2.23)–(2.25).

First, we test the discretization error in space. In order to do this, we choose a very small time step, e.g., $k = 0.0001$, such that the error from time discretization is negligible compared to the spatial discretization error, and solve the ZS with different methods under different mesh sizes h. Table 5.1 lists the numerical errors of e_1 and e_2 at $t = 2.0$ with different mesh sizes h for different numerical methods.

Second, we test the discretization error in time. Table 5.2 shows the numerical errors of e_1 and e_2 at $t = 2.0$ under different time steps k and mesh sizes h for different numerical methods.

Table 5.1
Spatial discretization error analysis: e_1, e_2 at time $t = 2$ under $k = 0.0001$.

	Mesh	$h = 1.0$	$h = \frac{1}{2}$	$h = \frac{1}{4}$
PSAS-TSSP	e_1	9.810E-2	1.500E-4	8.958E-9
	e_2	0.143	1.168E-3	6.500E-8
CN-LF-TSSP($\beta = 0$)	e_1	9.810E-2	1.500E-4	7.409E-9
	e_2	0.143	1.168E-3	3.904E-8
CN-LF-TSSP($\beta = 1/4$)	e_1	9.810E-2	1.500E-4	8.628E-9
	e_2	0.143	1.168E-3	6.521E-8
CN-LF-TSSP($\beta = 1/2$)	e_1	9.810E-2	1.500E-4	1.098E-8
	e_2	0.143	1.168E-3	6.326E-8

Table 5.2
Time discretization error analysis: e_1, e_2 at time $t = 2$.

	h	Error	$k = \frac{1}{100}$	$k = \frac{1}{400}$	$k = \frac{1}{1600}$	$k = \frac{1}{6400}$
PSAS-TSSP	$\frac{1}{4}$	e_1	4.968E-5	3.109E-6	1.944E-7	1.226E-8
		e_2	1.225E-4	7.664E-6	4.797E-7	3.871E-8
	$\frac{1}{8}$	e_1	4.968E-5	3.109E-6	1.944E-7	1.172E-8
		e_2	1.225E-4	7.664E-6	4.797E-7	3.157E-8
CN-LF-TSSP($\beta = 0$)	$\frac{1}{4}$	e_1	4.829E-5	3.022E-6	1.888E-7	1.156E-8
		e_2	1.032E-4	6.456E-6	4.041E-7	3.673E-8
	$\frac{1}{8}$	e_1	4.829E-5	3.022E-6	1.888E-7	1.100E-8
		e_2	1.032E-4	6.456E-6	4.043E-7	2.946E-8
CN-LF-TSSP($\beta = 1/4$)	$\frac{1}{4}$	e_1	5.679E-5	3.556E-6	2.224E-7	1.425E-8
		e_2	1.623E-4	1.015E-5	6.351E-7	4.970E-8
	$\frac{1}{8}$	e_1	5.679E-5	3.556E-6	2.224E-7	1.377E-8
		e_2	1.623E-4	1.015E-5	6.351E-7	4.356E-8
CN-LF-TSSP($\beta = 1/2$)	$\frac{1}{4}$	e_1	7.468E-5	4.678E-6	2.924E-7	1.868E-8
		e_2	2.232E-4	1.396E-5	8.732E-7	6.360E-8
	$\frac{1}{8}$	e_1	7.468E-5	4.678E-6	2.924E-7	1.841E-8
		e_2	2.232E-4	1.396E-5	8.732E-7	5.942E-8

Table 5.3
Conserved quantities analysis: $k = 0.0001$ and $h = \frac{1}{8}$.

	Time	e	D^{GZS}	P^{GZS}	H^{GZS}
PSAS-TSSP	1.0	8.943E-9	3.0000000000	3.41181556	0.510202736
	2.0	2.360E-8	3.0000000000	3.41181562	0.510202765
$\beta = 0$	1.0	7.281E-9	3.0000000000	3.41181557	0.510202736
	2.0	1.684E-8	3.0000000000	3.41181562	0.510202766
$\beta = 1/4$	1.0	1.053E-8	3.0000000000	3.41181556	0.510202740
	2.0	3.028E-8	3.0000000000	3.41181564	0.510202779
$\beta = 1/2$	1.0	1.206E-8	3.0000000000	3.41181556	0.510202737
	2.0	3.131E-8	3.0000000000	3.41181562	0.510202768

Third, we test the conservation of conserved quantities. Table 5.3 presents the quantities and numerical errors at different times with mesh size $h = \frac{1}{8}$ and time step $k = 0.0001$ for different numerical methods.

Case II. "Subsonic limit" regime, i.e., $0 < \varepsilon \ll 1$, we choose $B = 1$ and $C = 1/2\varepsilon$ in (5.1), (5.2). Under this choice, the wavelength of the initial data (5.1) is $O(\varepsilon)$.

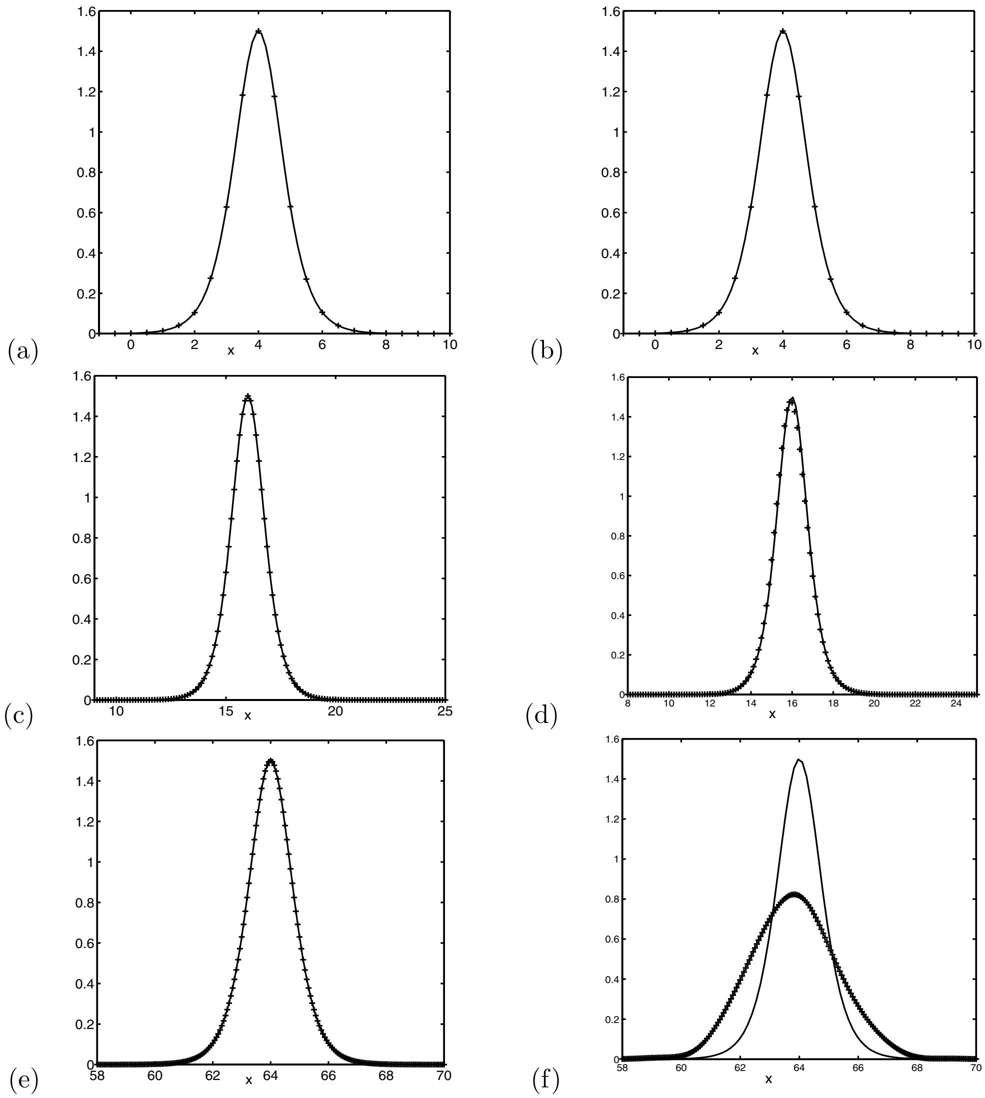

Fig. 1. *Numerical solutions of the electric field* $|E(x,t)|^2$ *at* $t = 1$ *for Example* 1 *in the subsonic limit regime by PSAS-TSSP. —: exact solution; + + +: numerical solution. The left column corresponds to* $h = O(\varepsilon)$ *and* $k = O(\varepsilon)$*:* (a) $\mathcal{T}_0 = (\varepsilon_0, h_0, k_0) = (0.125, 0.5, 0.04)$, (c) $\mathcal{T}_0/4$, (e) $\mathcal{T}_0/16$. *The right column corresponds to* $h = O(\varepsilon)$ *and* $k = 0.04$*—independent of* ε*:* (b) $\mathcal{T}_0 = (\varepsilon_0, h_0) = (0.125, 0.5)$, (d) $\mathcal{T}_0/4$, (f) $\mathcal{T}_0/16$.

Here we test the ε-resolution of different numerical methods. We solve the problem on the interval $[-8, 120]$, i.e., $a = -8$ and $b = 120$ with periodic boundary conditions. Figure 1 shows the numerical results of PSAS-TSSP at $t = 1$ when we choose the meshing strategy $h = O(\varepsilon)$ and $k = O(\varepsilon)$: $\mathcal{T}_0 = (\varepsilon_0, h_0, k_0) = (0.125, 0.5, 0.04)$, $\mathcal{T}_0/4$, $\mathcal{T}_0/16$; and $h = O(\varepsilon)$ and $k = 0.04$-independent of ε: $\mathcal{T}_0 = (\varepsilon_0, h_0) = (0.125, 0.5)$, $\mathcal{T}_0/4$, $\mathcal{T}_0/16$. CN-LF-TSSP with $\beta = 1/4$ or $\beta = 1/2$ gives similar numerical results at the same meshing strategies, where CN-LF-TSSP with $\beta = 0$ gives correct numerical results at meshing strategy $h = O(\varepsilon)$ and $k = O(\varepsilon^2)$, and incorrect results at $h = O(\varepsilon)$ and $k = O(\varepsilon)$ [6]. Furthermore, our additional numerical experiments confirm that

PSAS-TSSP and CN-LF-TSSP with $1/4 \le \beta \le 1/2$ are unconditionally stable, and CN-LF-TSSP with $\beta = 0$ is stable under the stability constraint (3.53).

From Tables 5.1–5.3 and Figure 1, we can draw the following observations.

In the $O(1)$-acoustic speed regime, our new methods PSAS-TSSP and CN-LF-TSSP with $\beta = 1/2$ or $1/4$ give similar results as the old method, i.e., CN-LF-TSSP with $\beta = 0$, proposed in [6]: they are of spectral-order accuracy in space discretization and second-order accuracy in time, they conserve D^{GZS} exactly and P^{GZS}, H^{GZS} very well (up to 8 digits). However, they are improved in two aspects: (i) They are unconditionally stable, where the old method is conditionally stable under the stability condition $k \le \frac{2h\varepsilon}{\pi\sqrt{d(1-4\beta)}}$ in d dimensions ($d = 1, 2$ or 3); (ii) in the "subsonic limit" regime, i.e., $0 < \varepsilon \ll 1$, the ε-resolution of our new methods is improved to $h = O(\varepsilon)$ and $k = O(\varepsilon)$, where the old method required $h = O(\varepsilon)$ and $k = O(\varepsilon h) = O(\varepsilon^2)$. Thus in the following, we present only numerical results by PSAS-TSSP. In fact, CN-LF-TSSP with $1/4 \le \beta \le 1/2$ gives similar numerical results at the same mesh size and time step for all the following numerical examples.

Example 2. The standard ZS with a plane-wave solution; i.e., we choose $d = 1$, $\varepsilon = 1$, $\alpha = 1$, $\lambda = 0$, $\gamma = 0$, and $\nu = -1$ in (1.1)–(1.3) and consider the problem on the interval $[a, b]$ with $a = 0$ and $b = 2\pi$. The initial condition is taken as

$$E(x, 0) = e^{i7x}, \quad N(x, 0) = 1, \quad \partial_t N(x, 0) = 0, \quad 0 \le x \le 2\pi. \tag{5.4}$$

It is easy to see that the ZS (3.1), (3.2) with the periodic boundary conditions (3.4), (3.5) and initial condition (5.4) admits the plane-wave solution (see [22])

$$E(x, t) = e^{i(7x-\omega t)}, \qquad \text{with} \quad \omega = 7^2 + 1 = 50, \tag{5.5}$$

$$N(x, t) = 1, \qquad a \le x \le b, \quad t \ge 0. \tag{5.6}$$

We solve this problem by using PSAS-TSSP on the interval $[0, 2\pi]$ with mesh size $h = \frac{\pi}{8}$ (i.e., 17 grid points in the interval $[0, 2\pi]$) and time step $k = 0.01$. Figure 2 shows the numerical results at $t = 2$ and $t = 4$.

From Figure 2, we can see that the time-splitting spectral method really provides the exact plane-wave solution of ZS.

5.2. Convergence in the subsonic limit regime ($0 < \varepsilon \ll 1$).

Example 3. Reduction from GZS to NLS and quadratic convergence rate in the subsonic limit regime; i.e., we choose $d = 1$, $\alpha = 1$, $\lambda = 0$, $\nu = -1$ in (2.21), (2.22), and (2.33). Let

$$E^0(x) = \operatorname{sech}(x+p)e^{-2i(x+p)} + \operatorname{sech}(x-p)e^{-2i(x-p)},$$
$$N^0(x) = -|\operatorname{sech}(x+p)|^2 - |\operatorname{sech}(x-p)|^2, \qquad -\infty < x < \infty.$$

We solve the GZS (2.21), (2.22) in one dimension with the initial conditions

$$E^{GZS}(x, 0) = E^0(x),\ N^{GZS}(x, 0) = N^0(x),\ \partial_t N^{GZS}(x, 0) = 0,\ -\infty < x < \infty,$$

and the NLS (2.33) in one dimension with the initial condition

$$E^{NLS}(x, 0) = E^0(x), \qquad -\infty < x < \infty,$$

in the interval $[-64, 64]$ with mesh size $h = \frac{1}{8}$ and time step $k = 0.0005$. We take $p = 10$. Let E^{GZS} and N^{GZS} be the numerical solutions of the GZS (2.21), (2.22),

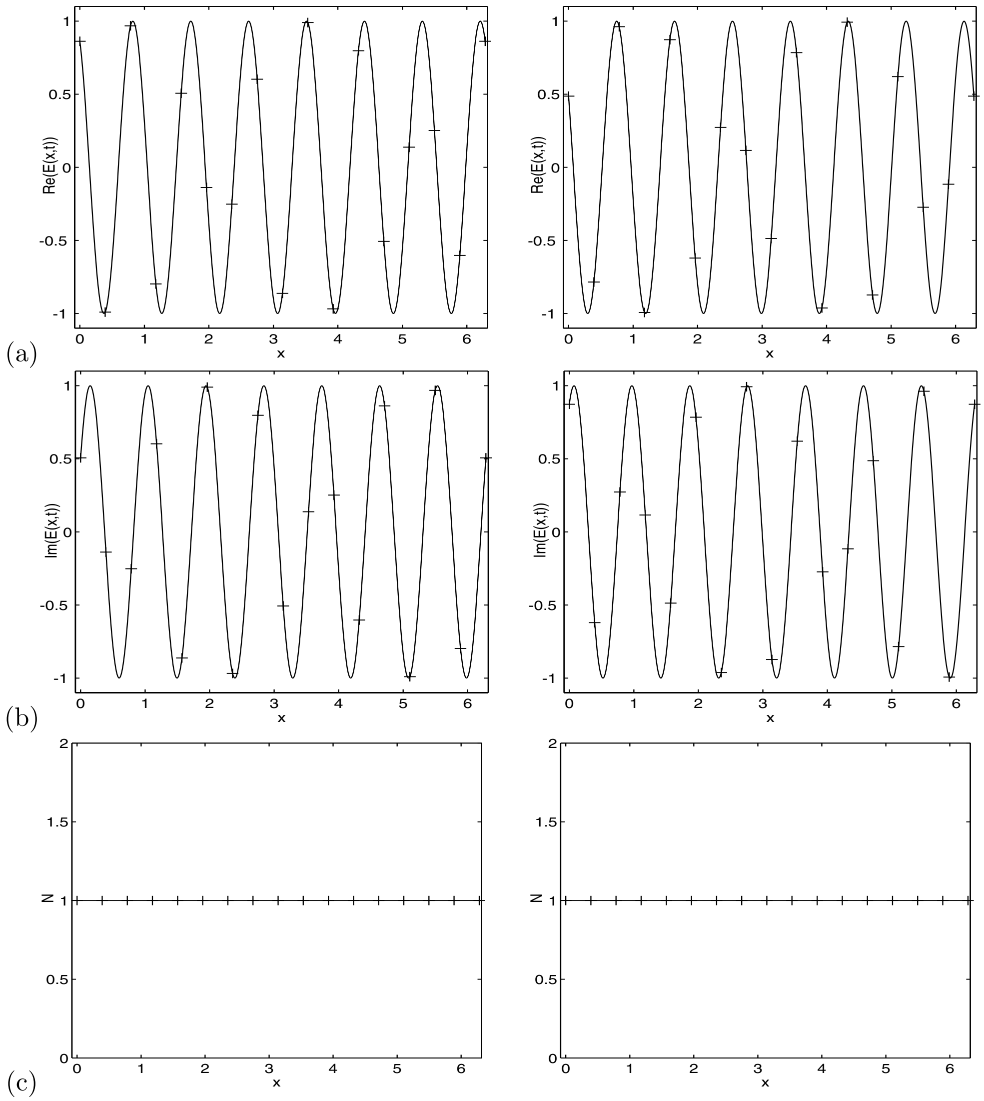

FIG. 2. *Numerical solutions at* $t = 2$ *(left column) and* $t = 4$ *(right column) in Example* 2. *—: exact solution given in* (5.5)–(5.6); *+ + +: numerical solution.* (a) $\mathrm{Re}(E(x,t))$*: real part of* E*,* (b) $\mathrm{Im}(E(x,t))$*: imaginary part of* E*,* (c) N*.*

and E^{NLS} of the NLS equation (2.33) by using PSAS-TSSP and TSSP [1, 3, 4], respectively. Table 5.4 shows the errors between the solutions of the GZS and its reduction NLS at time $t = 4.0$ under different ε.

From Table 5.4, we can see that the electron field E^{GZS}, ion density fluctuation N^{GZS}, electron density $|E^{GZS}|^2$, and the Hamiltonian H^{GZS} of the GZS (2.21), (2.22) converge to E^{NLS} in l^2-norm, $\nu|E^{NLS}|^2$ in l^2-norm, $|E^{NLS}|^2$ in l^1-norm, and H^{NLS} of the NLS (2.33) quadratically in the subsonic limit regime, i.e., $0 < \varepsilon \ll 1$, respectively, which confirms the formal analysis in (2.32), (2.38). In contrast, when $\varepsilon = O(1)$, the solutions of the GZS are far away from the solution of the NLS.

Example 4. Reduction from VZSM to GVZS and quadratic convergence rate in the subsonic limit regime; i.e., we choose $d = 1$, $\mathcal{M} = 2$, $a = 1$, $\alpha = -2$, $\gamma = 0$,

Table 5.4
Error analysis between GZS and its reduction NLS: Errors are computed at time $t = 4$ under $h = \frac{1}{8}$ and $k = 0.0005$.

	$\varepsilon = 1/80$	$\varepsilon = 1/40$	$\varepsilon = 1/20$	$\varepsilon = 1/10$	$\varepsilon = 1.0$
$\|E^{GZS} - E^{NLS}\|_{l^2}$	9.18E-3	3.66E-2	1.57E-1	7.04E-1	2.53
$\|N^{GZS} - \nu\|E^{NLS}\|^2\|_{l^2}$	8.10E-3	1.18E-1	2.54E-1	6.83E-1	1.78
$\|\|E^{GZS}\|^2 - \|E^{NLS}\|^2\|_{l^1}$	7.81E-3	3.17E-2	1.34E-1	6.95E-1	2.77
$\|H^{GZS} - H^{NLS}\|$	1.66E-6	1.52E-5	6.95E-5	4.58E-4	4.23E-2

$\varepsilon = \varepsilon_1 = 1.0$, $\nu = \nu_1 = 2.0$, $\nu_2 = 1.0$ in (4.1), (4.2) (with $\lambda = 0$) and (2.11), (2.12) (with $\lambda = 2\nu_2$). Denote the one-soliton solution of the GZS (2.21), (2.22) in one dimension as [6, 18, 19]

$$E_s(x,t;\eta,V,\varepsilon,\nu) = \left[\frac{\lambda}{2} + \frac{\nu}{\varepsilon^2}\left(\frac{1}{\varepsilon^2} - V^2\right)^{-1}\right]^{-1/2} U_s(x,t), \tag{5.7}$$

$$U_s(x,t) \equiv 2i\eta \operatorname{sech}[2\eta(x - Vt)] \exp\left[\frac{iVx}{2} + i\left(\frac{4\eta^2 - V^2}{4}\right)t + i\Phi_0\right], \tag{5.8}$$

$$N_s(x,t;\eta,V,\varepsilon,\nu) = \frac{\nu}{\varepsilon^2}\left(\frac{1}{\varepsilon^2} - V^2\right)^{-1} |E_s|^2, \tag{5.9}$$

where η and V are the soliton's amplitude and velocity and Φ_0 is a trivial phase constant. We solve the VZSM (2.4), (2.5) in one dimension for a two-component plasma with the initial conditions

$$E(x,0) = \sum_{r=\pm1} E_s(x + rp, 0, \eta_1, V_1, \varepsilon_1, \nu_1), \tag{5.10}$$

$$N_1(x,0) = \sum_{r=\pm1} N_s(x + rp, 0, \eta_1, V_1, \varepsilon_1, \nu_1), \tag{5.11}$$

$$\partial_t N_1(x,0) = \sum_{r=\pm1} \partial_t N_s(x + rp, 0, \eta_1, V_1, \varepsilon_1, \nu_1), \tag{5.12}$$

$$N_2(x,0) = \nu_2 \sum_{r=\pm1} |E_s(x + rp, 0, \eta_1, V_1, \varepsilon_1, \nu_1)|^2, \tag{5.13}$$

$$\partial_t N_2(x,0) = \nu_2 \sum_{r=\pm1} \partial_t |E_s(x + p, 0, \eta_1, V_1, \varepsilon_1, \nu_1)|^2, \tag{5.14}$$

and the GZS (2.21), (2.22) in one dimension with the initial conditions

$$\begin{aligned}
E^{GZS}(x,0) &= E_s(x + p, 0, \eta_1, V_1, \varepsilon, \nu) + E_s(x - p, 0, \eta_2, V_2, \varepsilon, \nu),\\
N^{GZS}(x,0) &= N_s(x + p, 0, \eta_1, V_1, \varepsilon, \nu) + N_s(x - p, 0, \eta_2, V_2, \varepsilon, \nu),\\
\partial_t N^{GZS}(x,0) &= \partial_t N_s(x + p, 0, \eta_1, V_1, \varepsilon, \nu) + \partial_t N_s(x - p, 0, \eta_2, V_2, \varepsilon, \nu)
\end{aligned}$$

in the interval $[-64, 64]$ with mesh size $h = \frac{1}{8}$ and time step $k = 0.0005$. Here $x = \mp p$ are the initial locations of the two solitons.

In our numerical simulations, we set $p = 10$, $\Phi_0 = 0$. We only simulated the symmetric collisions, i.e., the collisions of two solitons with equal amplitudes $\eta_1 = \eta_2 = \eta = 0.3$ and opposite velocities $V_1 = -V_2 \equiv V = 3.0$. Let E^{VZSM}, N_1^{VZSM}, and N_2^{VZSM} be the numerical solutions of the VZSM (2.4), (2.5), and E^{GVZS}, N^{GVZS} of the GVZS (2.21), (2.22) by using PSAS-TSSP. Table 5.5 shows the errors between the solutions of the VZSM and its reduction GVZS at time $t = 4.0$ under different ε_2.

Table 5.5

Error analysis between VZSM and its reduction GVZS: Errors are computed at time $t = 4$ under $h = \frac{1}{8}$ and $k = 0.0005$.

	$\varepsilon_2 = 1/80$	$\varepsilon_2 = 1/40$	$\varepsilon_2 = 1/20$	$\varepsilon_2 = 1$
$\|E^{VZSM} - E^{GVZS}\|_{l^2}$	1.06E-2	4.23E-2	1.76E-1	3.08
$\||E^{VZSM}|^2 - |E^{GVZS}|^2\|_{l^1}$	4.56E-3	1.85E-2	7.75E-2	2.41
$\|N_1^{VZSM} - N^{GVZS}\|_{l^2}$	4.87E-3	2.00E-2	8.67E-2	1.84
$\|N_2^{VZSM} - \nu_2|E^{GVZS}|^2\|_{l^2}$	2.29E-3	8.55E-3	3.82E-2	2.86

From Table 5.5, we can see that the electron field E^{VZSM}, electron density $|E^{VZSM}|^2$, ion density fluctuations N_1^{VZSM} and N_2^{VZSM}, of the VZSM (2.4), (2.5), converge to E^{GVZS} in l^2-norm, $|E^{GVZS}|^2$ in l^1-norm, N^{GVZS} and $\nu_2|E^{GVZS}|^2$ in l^2-norm, of the GVZS (2.21), (2.21), quadratically in the subsonic limit regime, i.e., $0 < \varepsilon_2 \ll 1$, respectively, which confirms the formal analysis in (2.10), (2.18). In contrast, when $\varepsilon_2 = O(1)$, the solutions of the VZSM are far away from the solution of the GVZS.

5.3. Applications.

Example 5. Two-dimensional GZS with a linear damping term; i.e., we choose $d = 2$ in (2.39), (2.40). Mathematically, when $H^{GZS} < 0$ in (2.25), the GZS (2.21), (2.22) will blow up at finite time. For fixed $E(\mathbf{x}, 0)$ and $N(\mathbf{x}, 0) = \nu|E(\mathbf{x}, 0)|^2$, there are three typical cases such that $H^{GZS} < 0$: (i) $\alpha = 1$, $\varepsilon = O(1)$, $\nu = -1$, $\lambda \gg 1$; (ii) $\lambda = 0$, $\varepsilon = O(1)$, $\nu = -1$, and $\alpha \gg 1$; (iii) $\alpha = 1$, $\lambda = 0$, $\nu \ll -1$, and $0 < \varepsilon \ll 1$. For this reason, here we present computations of the GZS (2.39), (2.40) with a linear damping term for three cases:

$$\begin{aligned}
&\text{Case I.} \quad \alpha = 1, \quad \lambda = 20, \quad \varepsilon = 1, \quad \nu = -1;\\
&\text{Case II.} \quad \alpha = 20, \quad \lambda = 0, \quad \varepsilon = 1, \quad \nu = -1;\\
&\text{Case III.} \quad \alpha = 1, \quad \lambda = 0, \quad \varepsilon = 0.1, \quad \nu = -20.
\end{aligned}$$

The initial conditions are taken as

$$E(x, y, 0) = \frac{1}{\sqrt{\pi}}\, e^{-\frac{x^2+y^2}{2}}, \qquad N(x, y, 0) = \frac{\nu}{\pi}\, e^{-(x^2+y^2)}, \qquad \partial_t N(x, y, 0) = 0.$$

The above parameters and initial conditions are chosen such that the initial Hamiltonian $H^{GZS} < 0$. Thus the GZS (2.21), (2.22) will blow up at finite time without damping.

We solve the damped GZS (2.39), (2.40) on the rectangle $[-4, 4]^2$ with mesh size $h = \frac{1}{32}$ and time step $k = 0.001$ for Cases I and II, and on $[-10, 10]^2$ with $h = \frac{5}{64}$ and $k = 0.0001$ for Case III. In our computations, two different damping parameters are chosen: (i) $\gamma = 0.8$ (arrest blowup), (ii) $\gamma = 0.1$ (can't arrest blowup).

Figure 3 shows the surface plots of electron density $|E|^2$ and ion density fluctuation N at different times and time evolution of the wave energy $D(t) := D^{GZS}(t)$, Hamiltonian $H(t) := H^{GZS}(t)$, central ion density fluctuation $N(0, 0, t)$, and central electron density $|E(0, 0, t)|^2$ with $\gamma = 0.8$ and 0.1 for Case I. In the numerical computations, a blowup is detected either from the plot of the central density $|E(0, 0, t)|^2$, which at the blowup shows a very sharp spike with a peak value that increases when the mesh size h decreases, or from the plot of the Hamiltonian $H(t)$, which has a very sharp spike with possible negative values at the blowup. In fact, the method

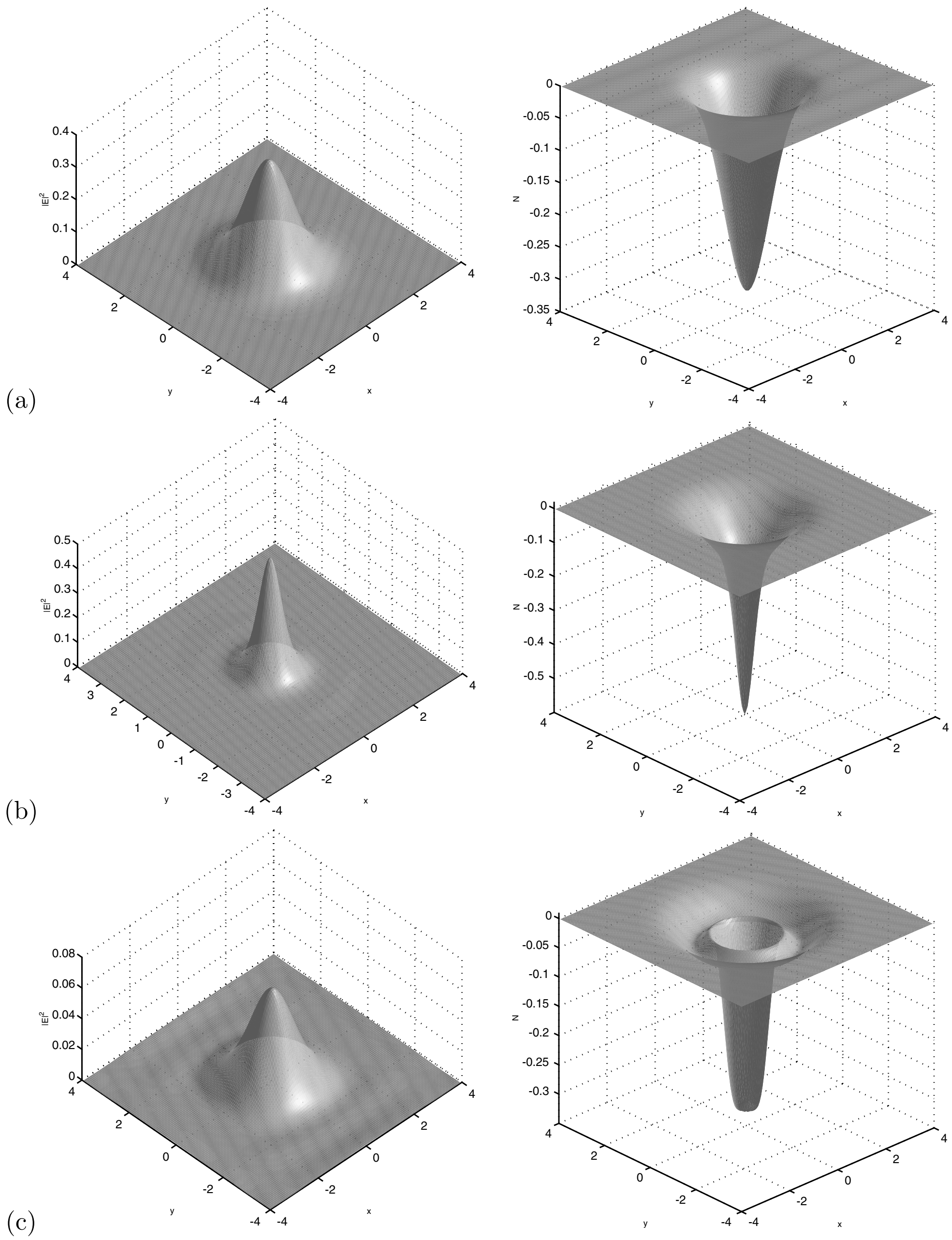

FIG. 3. *Surface-plot of the electron density* $|E(x,y,t)|^2$ *and ion density fluctuation* $N(x,y,t)$ *in Example* 3 *for Case* I (i) $\gamma = 0.8$ *at times:* (a) $t = 0$, (b) $t = 0.5$, (c) $t = 1.0$.

PSAS-TSSP (4.7), (4.8) aims to capture the solution of damped GZS or VZSM without blowup, i.e., the physically relevant solution. If one wants to capture the blowup rate of GZS or VZSM, we refer to [20, 23]. Similar graphics are obtained for Cases II and III; we have omitted them here.

From Figure 3, we can draw the following observations. (i) The GZS will blow up in certain parameter regimes, and the initial Hamiltonian $H^{GZS} < 0$. (ii) A linear

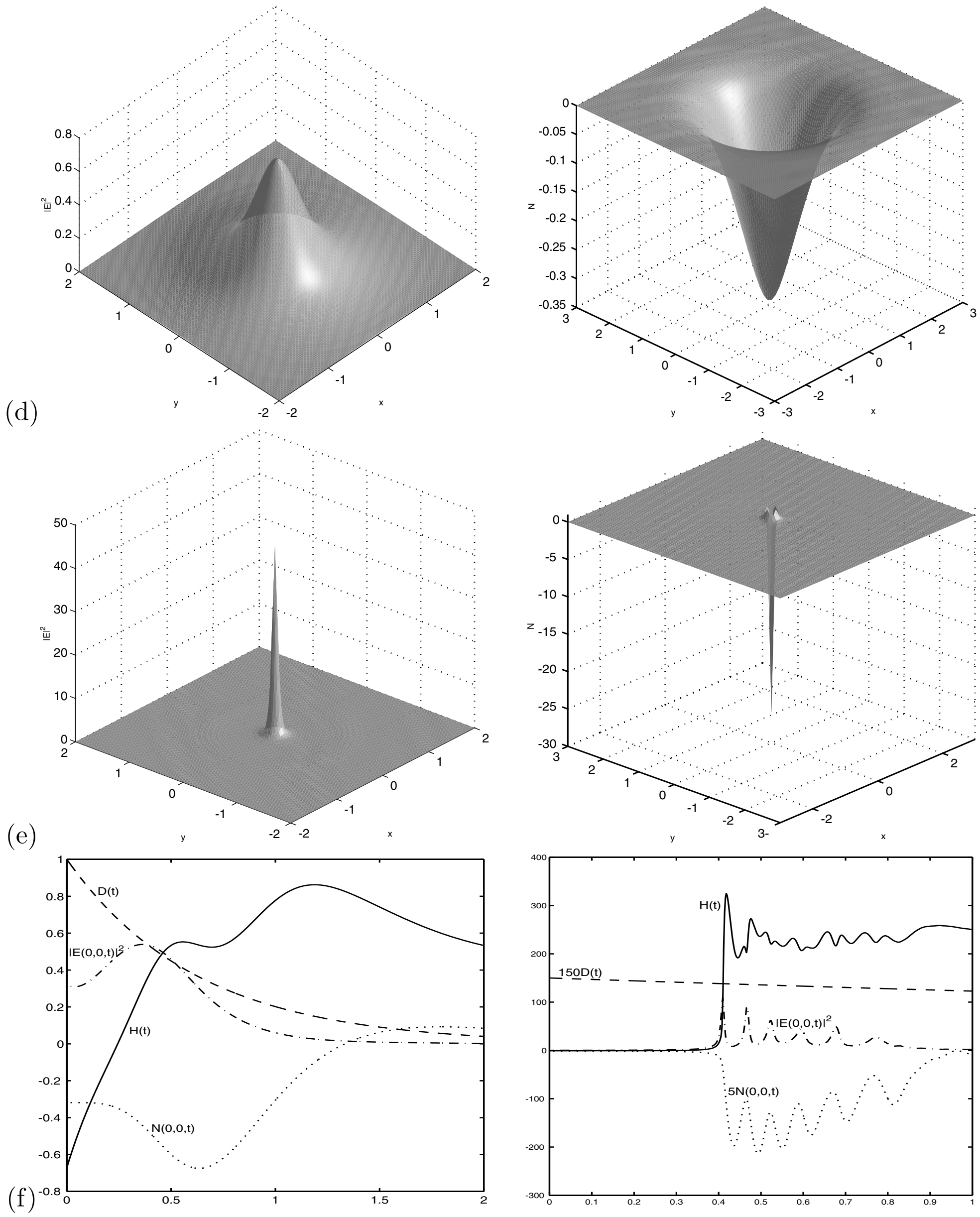

FIG. 3. *(Cont'd.)* (ii) $\gamma = 0.1$ *at times:* (d) *before blowup* ($t = 0.2$), (e) *after blowup* ($t = 0.473$), *and* (f) *time evolution of the wave energy* $D(t)$*, Hamiltonian* $H(t)$*, central ion density fluctuation* $N(0,0,t)$*, and central electron density* $|E(0,0,t)|^2$ *for different damping parameters:* $\gamma = 0.8$ *(left column: arrest blowup),* $\gamma = 0.1$ *(right column: blowup).*

damping can arrest blowup of GZS when the damping parameter γ is bigger than a threshold value $\gamma_{\rm th} > 0$ (cf. Figure 3(c) and (e)). (iii) When the blowup is arrested (cf. Figure 3(a), (b), and (c)), the pattern of the physically relevant solutions is the following: Initially the cloud contracts and the contraction is accompanied by an increase in the Hamiltonian (cf. Figure 3(f)). After the central electron density has reached a maximum, the cloud starts to expand due to the kinetic energy gained by the electrons during the contraction. The loss rate of the electrons from the cloud is independent of the shape of the density function, because the linear damping term is used. (iv) The wave energy decays to zero exponentially (cf. Figure 3(f)). Similar conclusions can be observed for Cases II and III.

Example 6. Soliton-soliton collisions in one-dimensional GZS; i.e., we choose $d = 1$, $\varepsilon = 1$, $\alpha = -2$, and $\gamma = 0$ in (1.1)–(1.3). We use the family of one-soliton solutions (5.7)–(5.9) in [18] to test our new numerical method PSAS-TSSP. The initial data is chosen as

$$\begin{aligned}
&E(x,0) = E_s(x+p,0,\eta_1,V_1,\varepsilon,\nu) + E_s(x-p,0,\eta_2,V_2,\varepsilon,\nu),\\
&N(x,0) = N_s(x+p,0,\eta_1,V_1,\varepsilon,\nu) + N_s(x-p,0,\eta_2,V_2,\varepsilon,\nu),\\
&\partial_t N(x,0) = \partial_t N_s(x+p,0,\eta_1,V_1,\varepsilon,\nu) + \partial_t N_s(x-p,0,\eta_2,V_2,\varepsilon,\nu),
\end{aligned}$$

where $x = \mp p$ are initial locations of the two solitons.

In all the numerical simulations reported in this example, we set $\lambda = 2$ and $\Phi_0 = 0$. We simulated only the symmetric collisions, i.e., the collisions of solitons with equal amplitudes $\eta_1 = \eta_2 = \eta$ and opposite velocities $V_1 = -V_2 \equiv V$. Here, we present computations for two cases:

Case I. *collision between solitons moving with the subsonic velocities,* $V < 1/\varepsilon = 1$; i.e., we take $\nu = 0.2$, $\eta = 0.3$, and $V = 0.5$;

Case II. *collision between solitons in the transonic regime,* $V > 1/\varepsilon = 1$; i.e., we take $\nu = 2.0$, $\eta = 0.3$, and $V = 3.0$.

We solve the problem on the interval $[-128, 128]$, i.e., $a = -128$ and $b = 128$ with mesh size $h = \frac{1}{4}$ and time step $k = 0.005$. We take $p = 10$. Figure 4 shows the evolution of the dispersive wave field $|E|^2$ and the acoustic (nondispersive) field N.

Case I corresponds to a soliton-soliton collision when the ratio ν/λ is small, i.e., the GZS (3.1), (3.2) is close to the NLS equation. As is seen, the collision seems quite elastic (cf. Figure 4(a)). This also validates the formal reduction from GZS to NLS in section 2.5. Case II corresponds to the collision of two transonic solitons. Note that the emission of the sound waves is inconspicuous at this value of V (cf. Figure 4(b)).

From Figure 4, we can see that the unconditionally stable numerical method PSAS-TSSP can really be applied to solving solitary-wave collisions of GZS.

Example 7. Soliton-soliton collisions in one-dimensional VZSM for a two-component plasma; i.e., we choose $\mathcal{M} = 2$, $d = 1$, $\gamma = 0$ in (4.1), (4.2). We use the family of one-soliton solutions (5.7)–(5.9) to test our method PSAS-TSSP. The initial data is chosen as (5.10)–(5.14).

In the numerical simulations in this example, we take $\lambda = 2\nu_2$, $p = 10$, and $\Phi_0 = 0$ in (5.8). Here we have only simulated the symmetric collisions, i.e., the collisions of two solitons with equal amplitudes $\eta_1 = \eta_2 = \eta$ and opposite velocities $V_1 = -V_2 \equiv V$. We present computations for four cases:

Case I. $\varepsilon_1 = 1$, $\nu_1 = 0.2$, $\eta = 0.3$, $V = 0.5$; $\varepsilon_2 = 0.1$, $\nu_2 = 1$, $\eta = 0.3$, $V = 0.5$;

Case II. $\varepsilon_1 = 1$, $\nu_1 = 0.2$, $\eta = 0.3$, $V = 0.5$; $\varepsilon_2 = 1$, $\nu_2 = 1$, $\eta = 0.3$, $V = 0.5$;

Case III. $\varepsilon_1 = 1$, $\nu_1 = 2$, $\eta = 0.3$, $V = 3$; $\varepsilon_2 = 0.1$, $\nu_2 = 1$, $\eta = 0.3$, $V = 3$;

Case IV. $\varepsilon_1 = 1$, $\nu_1 = 2$, $\eta = 0.3$, $V = 3$; $\varepsilon_2 = 1$, $\nu_2 = 1$, $\eta = 0.3$, $V = 3$.

In Cases I and II, the speed of the solitons $V < 1$, while in Cases III and IV, $V > 1$. In Cases I and III, the ratio between the acoustic speeds of the two components is much bigger than 1, while in Cases II and IV, it is at $O(1)$.

We solve the problem (4.1), (4.2) on the interval $[-128, 128]$ with mesh size $h = \frac{1}{4}$ and time step $k = 0.005$ by using the PSAS-TSSP. Figure 5 shows the evolution of the electron density $|E|^2$ for Cases I–IV.

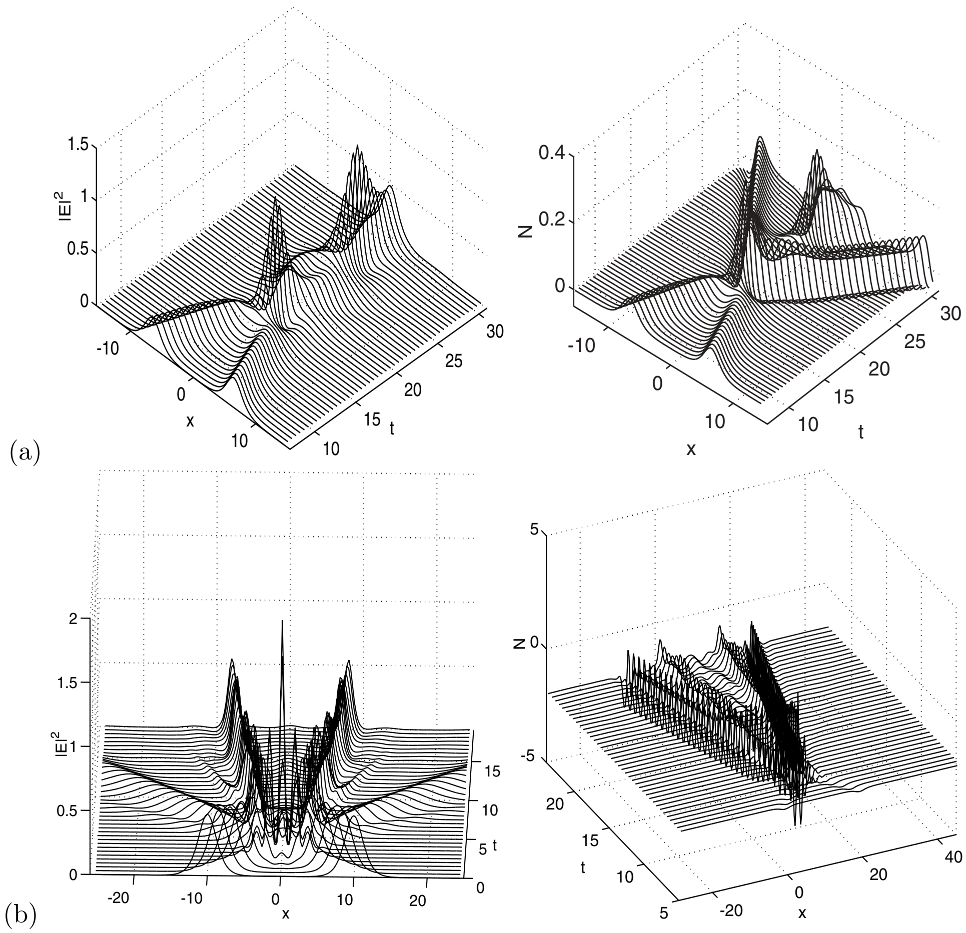

FIG. 4. *Evolution of the wave field* $|E|^2$ *(left column) and acoustic field* N *(right column) in Example* 6 *for* (a) *case* I, (b) *case* II.

Case I corresponds to a collision between solitons moving with subsonic velocities, i.e., $V < 1/\varepsilon_1 = 1 \ll 1/\varepsilon_2$, in a two-component plasma with two far different acoustic modes; i.e., the VZSM (4.1), (4.1) is close to the GZS (1.1), (1.2). Here the ratio $\nu_1/\lambda \ll 1$, i.e., the VZSM (4.1), (4.2) is also close to the NLS. As is seen, the collision seems quite elastic (cf. Figure 5(a)). Case II is similar to Case I except that we decrease the acoustic speed of the second component to the same order of the first component ($V < 1/\varepsilon_1 = 1/\varepsilon_2 = 1$); i.e., the VZSM (4.1), (4.2) is not close to the GZS (1.1), (1.2). We can see that the collision in this case is different from Case I (cf. Figure 5(a) and (b)). Case III corresponds to a collision of transonic solitons, i.e., $1/\varepsilon_1 = 1 < V \ll 1/\varepsilon_2$; i.e., the VZSM (4.1), (4.2) is close to the GZS (1.1), (1.2). The appearing solitons demonstrate irregular oscillations in their amplitude and size; the oscillations are accompanied a conspicuous emission of acoustic waves and inconspicuous emission of sound waves (cf. Figure 5(c)). Case IV is similar to Case III except that we decrease the acoustic speed of the second component to the same order of the first component ($1/\varepsilon_1 = 1/\varepsilon_2 = 1 < V$); i.e., the VZSM (4.1), (4.2) is not close to the GZS (1.1), (1.2). We can see that the collision in this case

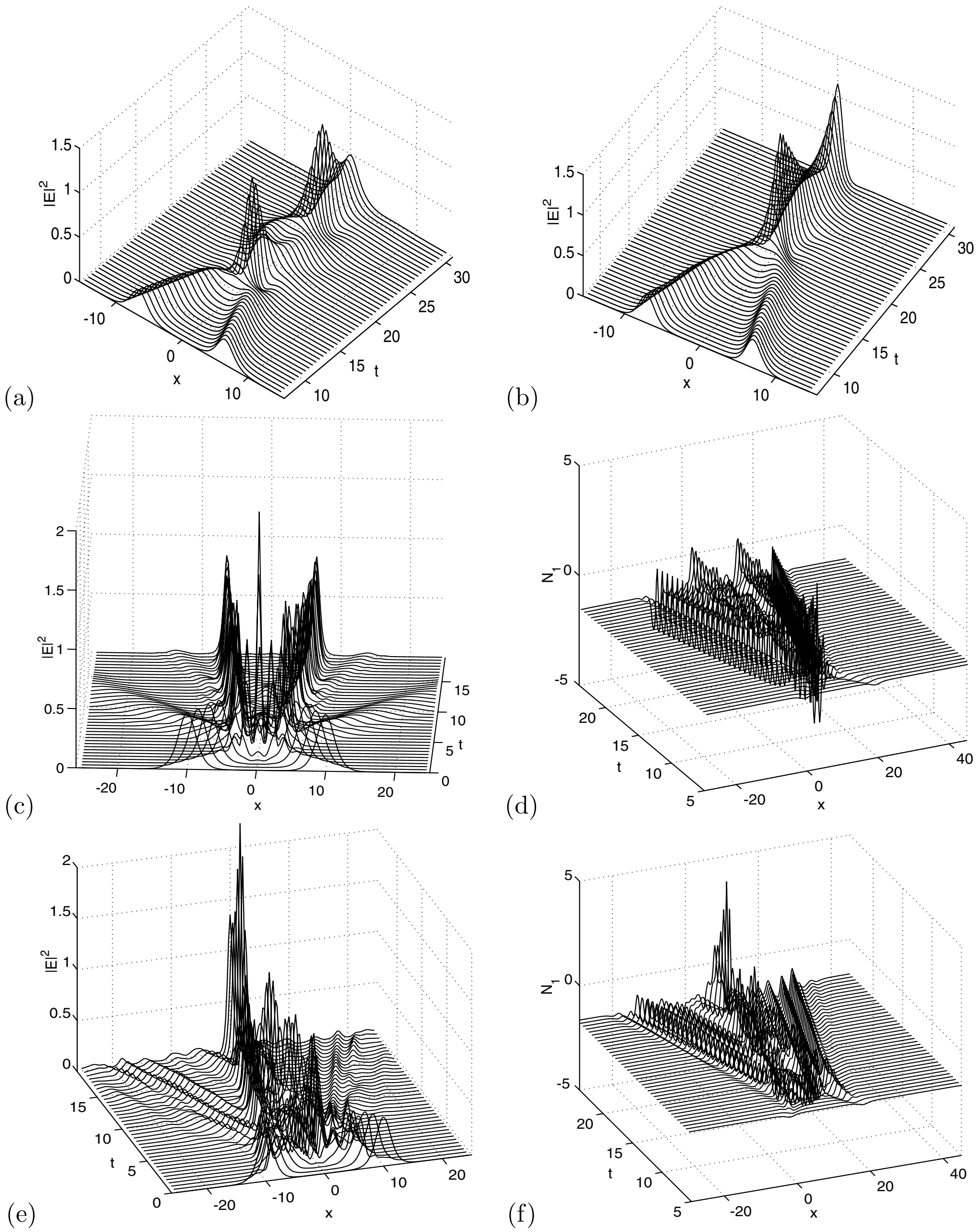

FIG. 5. *Evolution of the electron density* $|E|^2$ *and the ion density fluctuations* N_1 *in Example* 7 *for different cases:* (a) *Case I*, (b) *Case II*, (c) *and* (d) *Case III*, (e) *and* (f) *Case IV*.

is totally different from Case III (cf. Figure 5(c) and (d)). Comparing the results in this example for VZSM with the soliton-soliton collisions of Example 5 in [6, 29] of GZS for a single-component plasma, we can see that the collisions in Cases I and III for VZSM are close to the collisions of GZS for a single-component plasma. This also validates the formal reduction from VZSM to GVZS in section 2.2.

Example 8. Dynamics of three dimensions VZS; i.e., we choose $\mathcal{M}=1$, $d=3$, $a=2$, $\alpha=1$, $\lambda=0$, $\gamma=0$, $\nu_1=-1$, and $\varepsilon_1=1$ in (4.1), (4.2). The initial conditions are taken as

$$E_j(x,y,z,0)=e^{2i(\lambda_1 x-\lambda_2 y+2\lambda_3 z)}(\gamma_{1j}\gamma_{2j}\gamma_{3j})^{\frac{1}{4}}\frac{e^{-\frac{1}{2}(\gamma_{1j}x^2+\gamma_{2j}y^2+\gamma_{3j}z^2)}}{\sqrt{3}\pi^{3/4}},\quad j=1,2,3,$$
$$N(x,y,z,0)=e^{-2(x^2+y^2+z^2)},\qquad \partial_t N(x,y,z,0)\equiv 0;$$

with

$$\gamma_{11}=1,\ \gamma_{21}=2,\ \gamma_{31}=4;\quad \gamma_{12}=4,\ \gamma_{22}=2,\ \gamma_{32}=1;\quad \gamma_{13}=2,\ \gamma_{23}=4,\ \gamma_{33}=1.$$

We solve the VZS for two different initial parameters:

Case I. Zero initial phase data, i.e., $\lambda_1=\lambda_2=\lambda_3=0$.

Case II. Nonzero initial phase data, i.e., $\lambda_1=\lambda_2=\lambda_3=1$.

From (4.1), (4.2), after a simple analysis, we get

$$\begin{aligned}\frac{d}{dt}\|E_j(t)\|^2&=\frac{d}{dt}\int_{\mathbb{R}^d}|E_j(\mathbf{x},t)|^2\ d\mathbf{x}\\ &=2(a-1)\ \mathrm{Im}\int_{\mathbb{R}^d}\frac{\partial E_j}{\partial x_j}\ \nabla\cdot\overline{\mathbf{E}}\,d\mathbf{x},\quad t\ge 0,\ j=1,\dots,d.\end{aligned}\tag{5.15}$$

Plugging the above initial data into (5.15) at $t=0$, we obtain for Case I

$$\left.\frac{d||E_1(t)||^2}{dt}\right|_{t=0}=\left.\frac{d||E_2(t)||^2}{dt}\right|_{t=0}=\left.\frac{d||E_3(t)||^2}{dt}\right|_{t=0}=0,\tag{5.16}$$

and for Case II

$$\left.\frac{d||E_1(t)||^2}{dt}\right|_{t=0}>0,\qquad \left.\frac{d||E_2(t)||^2}{dt}\right|_{t=0}>0,\qquad \left.\frac{d||E_3(t)||^2}{dt}\right|_{t=0}<0.\tag{5.17}$$

In the two cases, the wave energy for each component of the electron field at time $t=0$ is set to be the same.

We solve the problem in the box $[-16,16]^3$ with mesh size $h=\frac{1}{4}$ and the time step $k=0.001$. Figure 6 shows the time evolution of the total wave energy $||\mathbf{E}(t)||_{l^2}^2$ and the wave energy of the three components of the electric field $||E_1(t)||_{l^2}^2$, $||E_2(t)||_{l^2}^2$, $||E_3(t)||_{l^2}^2$ for the two cases.

From Figure 6, we can see that the total wave energy $||\mathbf{E}(t)||_{l^2}^2$ is conserved in the two cases. In Case I, the conservation of the wave energy of the third component of the electron field is due to the symmetry of the initial data. The result in (5.16) is confirmed (cf. Figure 6(a)), and the wave energy of the first component increases after a short period; on the other hand, the wave energy of the second component decreases in order to conserve the total wave energy. In Case II, the result of (5.17) is confirmed (cf. Figure 6(b)), and time evolution of the wave energy for the first two components forms almost the same pattern (increasing-decreasing-increasing), where the pattern for the third component is opposite due to conservation of the total wave energy. The wave energy fluctuation is much larger in Case II than in Case I due to the nonzero initial phase in the electron field. Furthermore, the wave energy for each component almost does not change after some time. This implies that the electron does not exchange from one component to another after some time.

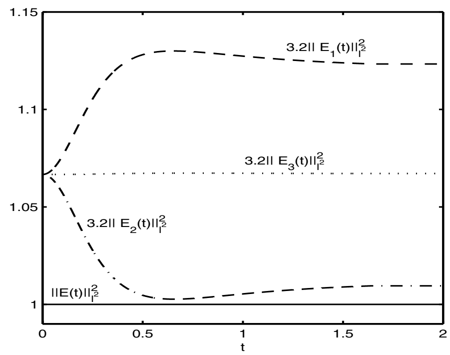

(a)

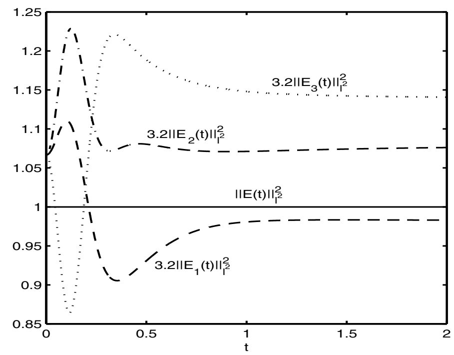

(b)

FIG. 6. *Evolution of the total wave energy* $||\mathbf{E}(t)||_{l^2}^2$ *and the wave energy of the three components of the electric field* $||E_1(t)||_{l^2}^2$, $||E_2(t)||_{l^2}^2$, $||E_3(t)||_{l^2}^2$ *in Example* 8 *for* (a) *Case* I, (b) *Case* II.

6. Conclusions. New efficient and stable numerical methods PSAS-TSSP and CN-LF-TSSP with $1/4 \leq \beta \leq 1/2$ are presented for the generalized Zakharov system (GZS) and vector Zakharov system for multicomponent (VZSM). The methods are explicit, unconditionally stable, easy to extend to high dimensions, easy to program, less memory-demanding, and time reversible and time transverse invariant when there is no damping term in GZS or VZSM. Furthermore, they keep the same decay rate of the wave energy in GZS or VZSM, and give exact results for plane-wave solutions of GZS. Numerical results for a solitary-wave solution demonstrate that the methods are of spectral-order accuracy in space and second-order accuracy in time and also possess "optimal" ε-resolution in the "subsonic limit" regime (i.e., $0 < \varepsilon \ll 1$) with the following meshing strategy: mesh size $h = O(\varepsilon)$ and time step $k = O(\varepsilon)$. The methods are then applied successfully to simulate solitary-wave collisions of GZS as well as a three-dimensional problem. From our numerical results, we observe (i) a quadratic convergence rate of VZSM to GZS in the "subsonic limit" regime; (ii) a quadratic convergence rate of GZS to NLS in the "subsonic limit" regime; (iii) that a linear damping can arrest blowup in GZS or VZSM when the damping parameter γ is bigger than a threshold value $\gamma_{\text{th}} > 0$; and (iv) that nonelastic collisions between solitons may appear in GZS or VZSM. Moreover, when the initial data for GZS or VZSM decays to zero sufficiently fast when $|\mathbf{x}| \to \infty$, which can be approximated by homogeneous Dirichlet boundary conditions, in general, we recommend using PSAS-TSSP with a sine-basis function for numerical discretization of GZS or VZSM.

In [5], the PSAS-TSSP is extended to the Maxwell–Dirac system for time-evolution of fast (relativistic) electrons and positrons within self-consistent generated electromagnetic fields.

REFERENCES

[1] W. Bao and D. Jaksch, *An explicit unconditionally stable numerical method for solving damped nonlinear Schrödinger equations with a focusing nonlinearity*, SIAM J. Numer. Anal., 41 (2003), pp. 1406–1426.

[2] W. Bao, D. Jaksch, and P.A. Markowich, *Numerical solution of the Gross–Pitaevskii equation for Bose–Einstein condensation*, J. Comput. Phys., 187 (2003), pp. 318–342.

[3] W. Bao, S. Jin, and P.A. Markowich, *On time-splitting spectral approximations for the Schrödinger equation in the semiclassical regime*, J. Comput. Phys., 175 (2002), pp. 487–524.

[4] W. Bao, S. Jin, and P.A. Markowich, *Numerical study of time-splitting spectral discretizations of nonlinear Schrödinger equations in the semiclassical regimes*, SIAM J. Sci. Comput., 25 (2003), pp. 27–64.

[5] W. Bao and X.-G. Li, *An efficient and stable numerical method for the Maxwell–Dirac system*, J. Comput. Phys., 199 (2004), pp. 663–687.

[6] W. Bao, F.F. Sun, and G.W. Wei, *Numerical methods for the generalized Zakharov system*, J. Comput. Phys., 190 (2003), pp. 201–228.

[7] J. Bourgain, *On the Cauchy and invariant measure problem for the periodic Zakharov system*, Duke Math. J., 76 (1994), pp. 175–202.

[8] J. Bourgain and J. Colliander, *On well-posedness of the Zakharov system*, Internat. Math. Res. Notices, 11 (1996), pp. 515–546.

[9] Q. Chang and H. Jiang, *A conservative difference scheme for the Zakharov equations*, J. Comput. Phys., 113 (1994), pp. 309–319.

[10] Q. Chang, B. Guo, and H. Jiang, *Finite difference method for generalized Zakharov equations*, Math. Comp., 64 (1995), pp. 537–553.

[11] J. Colliander, *Well-posedness for Zakharov systems with generalized nonlinearity*, J. Differential Equations, 148 (1998), pp. 351–363.

[12] A.S. Davydov, *Solitons in molecular systems*, Phys. Scr., 20 (1979), pp. 387–394.

[13] L.M. Degtyarev, V.G. Nakhan'kov, and L.I. Rudakov, *Dynamics of the formation and interaction of Langmuir solitons and strong turbulence*, Sov. Phys. JETP, 40 (1974), pp. 264–268.

[14] J. Ginibre, Y. Tsutsumi, and G. Velo, *The Cauchy problem for the Zakharov system*, J. Funct. Anal., 151 (1997), pp. 384–436.

[15] R. Glassey, *Approximate solutions to the Zakharov equations via finite differences*, J. Comput. Phys., 100 (1992), pp. 377–383.

[16] R. Glassey, *Convergence of an energy-preserving scheme for the Zakharov equations in one space dimension*, Math. Comp., 58 (1992), pp. 83–102.

[17] O. Goubet and I. Moise, *Attractor for dissipative Zakharov system*, Nonlinear Anal., 31 (1998), pp. 823–847.

[18] H. Hadouaj, B.A. Malomed, and G.A. Maugin, *Soliton-soliton collisions in a generalized Zakharov system*, Phys. Rev. A, 44 (1991), pp. 3932–3940.

[19] H. Hadouaj, B.A. Malomed, and G.A. Maugin, *Dynamics of a soliton in a generalized Zakharov system with dissipation*, Phys. Rev. A, 44 (1991), pp. 3925–3931.

[20] M.J. Landman, G.C. Papanicolaou, C. Sulem, P.L. Sulem, and X.P. Wang, *Stability of isotropic singularities for the nonlinear Schrödinger equation*, Phys. D, 47 (1991), pp. 393–415.

[21] V. Masselin, *A result of the blow-up rate for the Zakharov system in dimension* 3, SIAM J. Math. Anal., 33 (2001), pp. 440–447.

[22] P.K. Newton, *Wave interactions in the singular Zakharov system*, J. Math. Phys., 32 (1991), pp. 431–440.

[23] G.C. Papanicolaou, C. Sulem, P.L. Sulem, and X.P. Wang, *Singular solutions of the Zakharov equations for Langmuir turbulence*, Phys. Fluids B, 3 (1991), pp. 969–980.

[24] G.L. Payne, D.R. Nicholson, and R.M. Downie, *Numerical solution of the Zakharov equations*, J. Comput. Phys., 50 (1983), pp. 482–498.

[25] N.R. Pereira, *Collisions between Langmuir solitons*, Phys. Fluids, 20 (1977), pp. 750–755.

[26] L. Stenflo, *Nonlinear equations for acoustic gravity waves*, Phys. Scr., 33 (1986), pp. 156–158.

[27] C. Sulem and P.L. Sulem, *Regularity properties for the equations of Langmuir turbulence*, C. R. Acad. Sci. Paris Sér. A Math., 289 (1979), pp. 173–176.

[28] C. Sulem and P.L. Sulem, *The Nonlinear Schrödinger Equation*, Springer, New York, 1999.

[29] F.F. Sun, *Numerical Studies on the Zakharov System*, Masters thesis, Department of Computational Science, National University of Singapore, 2003.

[30] V.E. Zakharov, *Collapse of Langmuir waves*, Zh. Eksp. Teor. Fiz., 62 (1972), pp. 1745–1759 (translated from Sov. Phys. JETP, 35 (1972), pp. 908–914).